Crack identification with incomplete boundary data in linear elasticity by the reciprocity gap method

Renaud Ferrier, Mohamed Larbi Kadri, Pierre Gosselet

Computational Mechanics manuscript No.
(will be inserted by the editor)

Crack identification with incomplete boundary data in linear elasticity by the reciprocity gap method

R. Ferrier[1], **M. Kadri**[2], **P. Gosselet**[3]

[1] LMA, Université Aix-Marseille, 4 impasse Nikola Tesla, 13013 Marseille, France

[2] LAMSIN, ENIT, BP 37, 1002, Le Bélvédère, Tunis, Tunisia

[3] LaMcube, Université de Lille, Bâtiment ESPRIT, Cité Scientifique, Villeneuve-d'Ascq

Received: date / Revised version: date

Abstract This paper proposes and studies three methods for the identification of cracks in linear elastic bodies. They are based on the reciprocity gap principle which they extend to the case of partially redundant boundary data. The methods are all assessed on an academic 2D case, then the most appealing is more deeply analysed and illustrated on a 3D test-case.

Key words crack identification; reciprocity gap method; inverse problems; data completion; Newton algorithm

1 Introduction

Crack identification is an important issue in the context of the non-destructive control of in-situ mechanical parts. In this framework, we focus on the problem of reconstructing crack shapes from the measurement of displacement on a part of the boundary subjected to known static load. This question, which belongs to the class of inverse problems, has received much attention in the past years. In [8], the authors gave uniqueness and stability results for the emerging crack identification problem on the Laplace equation. In [10], uniqueness was proven for buried cracks, and stability for emerging cracks in elasticity. Both uniqueness results are true for unspecified shapes of the crack, while both stability results were proven for straight cracks. [24] proposed an identification method for the 2D Laplace equation based on the minimization of the Kohn-Vogelius functional.

Solving inverse problems often reduces to solving many forward problems, which is often very CPU-consuming. This why non-iterative methods have been investigated, such as the linear sampling method (for the Helmholtz equation) in [15] or the topological gradient method in [2].

In [6], the authors introduced the reciprocity gap method, which applies to homogeneous materials and does not rely on any forward resolution. In [7], a theoretical study of this method applied to crack identification was provided. Two main limitations must be underlined: first, it is required to know *both* Dirichlet and Neumann data on the *entire* boundary, and second, only plane cracks can be identified. In [19], a complete numerical study of the algorithm was provided, and a variant better suited to thick domains was proposed.

Many studies have been carried out about different versions of this method. In [11], the method is applied to the Helmholtz equation, which allows the identification of more complicated shapes. In [27], the authors proposed a generalization to piezo-electrical materials. In [25], an application of the reciprocity gap was proposed for small ellipsoidal inclusions. In a more recent paper [26], the authors proposed a method based on the reciprocity gap to identify small non-coplanar separated cracks. Some authors have already worked to relax the necessity of redundant data on all the boundary. One can mention [12], dealing with the 2D Laplace equation, where the missing boundary data was first completed via the resolution of a bounded extremal problem and the reciprocity gap was used in a second step. In [4], the authors made a numerical study of the algorithm of [7] on the particular case of an emerging crack in a known plane, with partially missing Dirichlet data recovered by solving a preliminary Cauchy problem.

In this work, we study three different ways to overcome the necessity of having complete redundant data. In Section 2, the general identification problem is presented, as well as a simple test-case to compare the methods. Section 3 is dedicated to the method proposed by [4], that consists in solving a preliminary Cauchy problem, with the Steklov-Poincaré method [18] in our case. This method will be referred to as Cauchy Reciprocity Gap (C-RG). In Section 4, we show that, in some cases, it is possible to generate test-fields adapted to the missing data, and the resulting method is referred to as Petrov-Galerkin-homogeneous Reciprocity Gap (PG0-RG). In Section 5, we present a method that simultaneously identifies the crack and the missing boundary value via the reciprocity gap method. We call this last method the general Petrov-Galerkin Reciprocity Gap (gPG-RG) The last section proposes a deeper numerical study of that last method on, among others, a 3D test-case.

2 Crack identification problem

Let $\Omega \subset \mathbb{R}^d$ ($d = 2$ or 3), be an open domain. Its boundary is denoted by $\partial\Omega$ and $\underline{n}$ is the outer-pointing normal vector. The domain has an internal crack, denoted by Σ, and $\underline{n}_\Sigma$ is the normal vector to this crack. We consider that this domain is subjected to a series of $r_{\max}$ self-equilibrated boundary traction loads $\left(\underline{f}_r\right)$. Let $\underline{u}_r$ be the displacement field, $\underline{\underline{\sigma}}_r$ the Cauchy stress tensor, $\mathbb{H}$ the Hooke's tensor and $\underline{\underline{\varepsilon}}$ the

symmetric gradient operator. The system of equations satisfied by $(\underline{u}_r, \underline{\underline{\sigma}}_r)$ can be written as:

$$\forall r,\ 1 \leqslant r \leqslant r_{\max},\quad \begin{aligned} \underline{0} &= \underline{\mathrm{div}}(\underline{\underline{\sigma}}_r) \ \text{ in } \ \Omega\backslash\Sigma, \\ \underline{\underline{\sigma}}_r &= \mathbb{H} : \underline{\underline{\varepsilon}}(\underline{u}_r) \ \text{ in } \ \Omega\backslash\Sigma, \\ \underline{\underline{\sigma}}_r \cdot \underline{n}_\Sigma &= \underline{0} \ \text{ on } \ \Sigma \\ \underline{\underline{\sigma}}_r \cdot \underline{n} &= \underline{f}_r \ \text{ on } \ \partial\Omega \end{aligned} \tag{1}$$

The solution to this system (1) is unique provided it is sought in the space orthogonal to the rigid body motions space. Note that these equations correspond to a simplistic representation of the crack since, without further assumptions, interpenetration would be possible. In the following, we will either assume that the loads are known to open the crack or we will improve the model by considering frictionless unilateral contact on the crack lips.

We set the notation $\underline{\underline{\sigma}}(\bullet) = \mathbb{H} : \underline{\underline{\varepsilon}}(\bullet)$. Let $\mathcal{V} = \{\underline{v} \in H^1(\Omega),\ \underline{\underline{\sigma}}(\underline{v}) \in H_{div}(\Omega),\ \underline{\mathrm{div}}(\underline{\underline{\sigma}}(\underline{v})) = \underline{0}$ weakly in $\Omega\}$, the set of elastically mechanical balanced test functions (mechanical equivalent to harmonic functions). The reciprocity gap functional RG_r is defined as follows:

$$\begin{aligned} \underline{v} \in \mathcal{V} &\mapsto \mathrm{RG}_r(\underline{v}) \in \mathbb{R} \\ &= \int_{\partial\Omega} (\underline{f}_r \cdot \underline{v} - \underline{u}_r \cdot \underline{\underline{\sigma}}(\underline{v}) \cdot \underline{n}) \,\mathrm{dS} \end{aligned} \tag{2}$$

If $[\![\underline{u}_r]\!]$ denotes the displacement jump on the crack, one can prove that:

$$\forall \underline{v} \in \mathcal{V},\ \mathrm{RG}_r(\underline{v}) = \int_\Sigma \underline{\underline{\sigma}}(\underline{v}) : (\underline{n}_\Sigma \otimes [\![\underline{u}_r]\!]) \,\mathrm{dS} \tag{3}$$

If the material's constitutive parameters, on which $\underline{\underline{\sigma}}$ depends, are homogeneous, functions in $\mathcal{V}$ can be computed numerically or analytically.

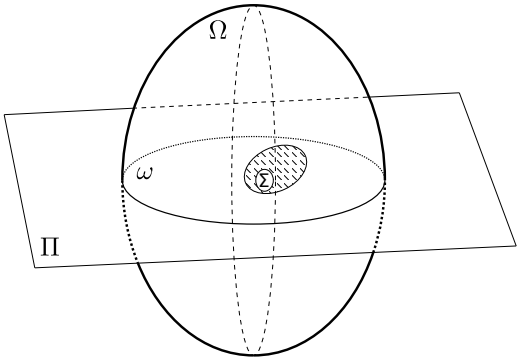

Fig. 1: Definition of the crack and its supporting surface

In the case when the displacement $\underline{u}_r$ and traction $\underline{f}_r$ fields are known on the whole boundary $\partial\Omega$, the right-hand side of (2) is fully known and the reciprocity gap method consists in computing $\mathrm{RG}_r(\underline{v})$ for well-chosen test-fields and to use this information to infer the shape of Σ. In particular, if we assume that the crack Σ is planar, contained in the plane written Π, two experiments ($r_{max} = 2$) and well-chosen test-fields enable to fully characterize the crack's plane Π [7]. The method remains valid in the case of several cracks belonging to the same plane Π, see for example [19] or [11] for Helmholtz equation.

The intersection of Π with the domain Ω is denoted by ω, as described on Figure 1. The equation (3) can then be re-written by using the extension by 0 of $[\![\underline{u}_r]\!]$ on ω:

$$\forall \underline{v} \in \mathcal{V},\ \mathrm{RG}_r(\underline{v}) = \int_\omega \underline{\underline{\sigma}}(\underline{v}) : (\underline{n}_\Pi \otimes [\![\underline{u}_r]\!]) \,\mathrm{dS} \tag{4}$$

Then, the Galerkin projection of (4) into a finite dimensional subspace enables to reconstruct an approximation of $[\![\underline{u}_r]\!]$. The shape of the crack can then be post-processed, for instance by thresholding.

This paper focuses on the cases where the displacement and traction fields are not known on the whole boundary. Let us introduce the following parts of the boundary $\partial\Omega$: Γ_n is the part where Neumann data $\underline{\widehat{f}}_r$ is available and Γ_d is the part where Dirichlet data $\underline{\widehat{u}}_r$ is available. The hat notation is reserved to quantities which are known because they are either imposed or measured. We note $\Gamma_{\bar{n}} = \partial\Omega \setminus \Gamma_n$ and $\Gamma_{\bar{d}} = \partial\Omega \setminus \Gamma_d$, when needed the unknown traction and displacement fields are written $\underline{\widetilde{f}}_r$ and $\underline{\widetilde{u}}_r$. The partition of the boundary is illustrated on Figure 2. The crack identification problem considered in this paper consists in recovering Σ from the knowledge of $\underline{\widehat{u}}_r$ and $\underline{\widehat{f}}_r$. One condition for the uniqueness of the solution to the crack identification problem is that $\text{meas}(\Gamma_n \cap \Gamma_d) \neq 0$.

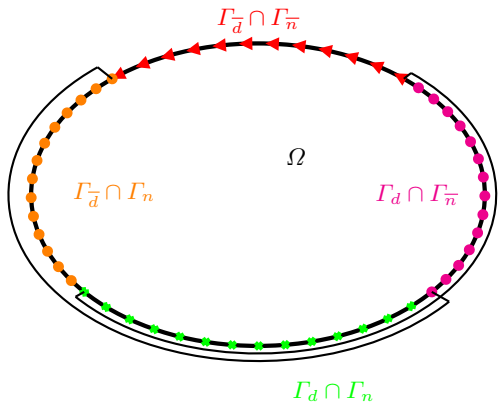

Fig. 2: Partition of the boundary of the domain

The missing knowledge on the boundary makes it impossible to use the standard RG procedure. In particular, it is impossible to directly characterize the plane containing the crack. Among the 3 procedures that we propose in the following sections, the first one (C-RG) tries to recover the missing boundary data before using the plain RG procedure. The other two methods embed the RG functional in minimization problems, which can be viewed as variations around the reciprocity likelihood maximization [3]. In these cases, the crack is still sought as the support of the displacement jump on a surface to be determined, but the assumed flatness can no more be exploited, so even curved cracks could be considered, as long as the surface remains simple to configure. In order to be able to compare all three methods and maintain computational cost low, we maintain the planar crack hypothesis in the whole paper.

For the first numerical illustrations, we study the case of a cracked unit square subjected to a zero Dirichlet boundary condition on its top side. Various Neumann loads are then applied on the other sides and the resulting displacement is measured. In this framework, Dirichlet data is available on the entire boundary ($\Gamma_d = \partial\Omega$) whereas the reaction forces on the top side are unknown ($\Gamma_{\bar{n}}$ is the top side, Γ_n is the three other sides). The load cases are presented on Figure 3, as said earlier, they all tend to open the crack.

3 Pre-processing by a data completion algorithm (C-RG)

In this part, the way to overcome the lack of knowledge on one of the sides is to first run a data completion algorithm to reconstruct the missing piece of

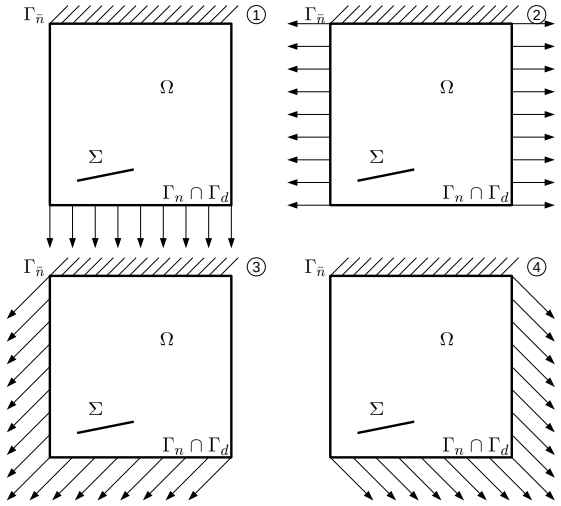

Fig. 3: Studied domain and applied load cases

information. This strategy has already been followed in [12,21].

3.1 Presentation of the method

We first solve a Cauchy problem on a smaller part of Ω, denoted by Ω_1 and assumed not to contain the crack, whose boundary contains all the partially known edges (faces in 3D) at a least a part of the fully known edges: $\partial\Omega \setminus (\Gamma_n \cap \Gamma_d) \subset \partial\Omega_1$ and $\partial\Omega_1 \cap (\Gamma_n \cap \Gamma_d) \neq \emptyset$. The interface $\Gamma = \partial\Omega_1 \cap \Omega$ closes the domain (see Figure 4). In the proposed example, the lateral sides belong to $\Gamma_n \cap \Gamma_d$, that is to say they bear redundant information, while the top side is only in Γ_d. The equations corresponding to the Cauchy problem are:

$$\begin{aligned}
&\underline{0} = \mathrm{div}(\underline{\underline{\sigma}}_r(\underline{u}_r)) \quad \text{in} \quad \Omega_1 \\
&\underline{\underline{\sigma}}_r = \mathbb{H} : \underline{\underline{\varepsilon}}(\underline{u}_r) \quad \text{in} \quad \Omega_1 \\
&\underline{\underline{\sigma}}_r \cdot \underline{n} = \widehat{\underline{f}}_r \quad \text{on} \quad \partial\Omega_1 \cap \Gamma_n \\
&\underline{u}_r = \widehat{\underline{u}}_r \quad \text{on} \quad \partial\Omega_1 \cap \Gamma_d
\end{aligned} \tag{5}$$

Many methods exist in the literature to solve this system. One can cite for example the energy error gap method from [5], the iterated regularization from [16] or the alternating method of [22]. We choose to use the Steklov-Poincaré algorithm [14], which has been successfully applied in the framework of crack identification in [21]. A recent study [18] convinced us to use the dual variant with a block conjugate gradient solver and Ritz filtering of the solution. The advantage of this approach is that thanks to the block solver [23], the Cauchy problems corresponding to all the load cases are solved simultaneously at almost no extra cost, and more Ritz values are computed per iteration, which means that fewer iterations are needed to process more data.

Once the data is completed, both displacement and normal stress fields are known on the whole boundary of Ω_1, in particular on the artificial interface Γ and on the top side $\Gamma_{\bar{n}}$. Two choices are thus possible for the crack identification, as illustrated on Figure 4. The first one consists in applying the reciprocity gap method on $\Omega_2 = \Omega \setminus \Omega_1$, by using the previously computed $\underline{f}$ and $\underline{u}$ on Γ. The second choice is to apply the reciprocity gap method on Ω thanks to the traction field $\underline{f}$ computed on the top side $\Gamma_{\overline{n}}$.

With the former choice, the crack identification is applied on a more slender domain, but with the latter choice, more accurate information is used since the displacement on the top side was a given quantity and only the reaction needed to be rebuilt.

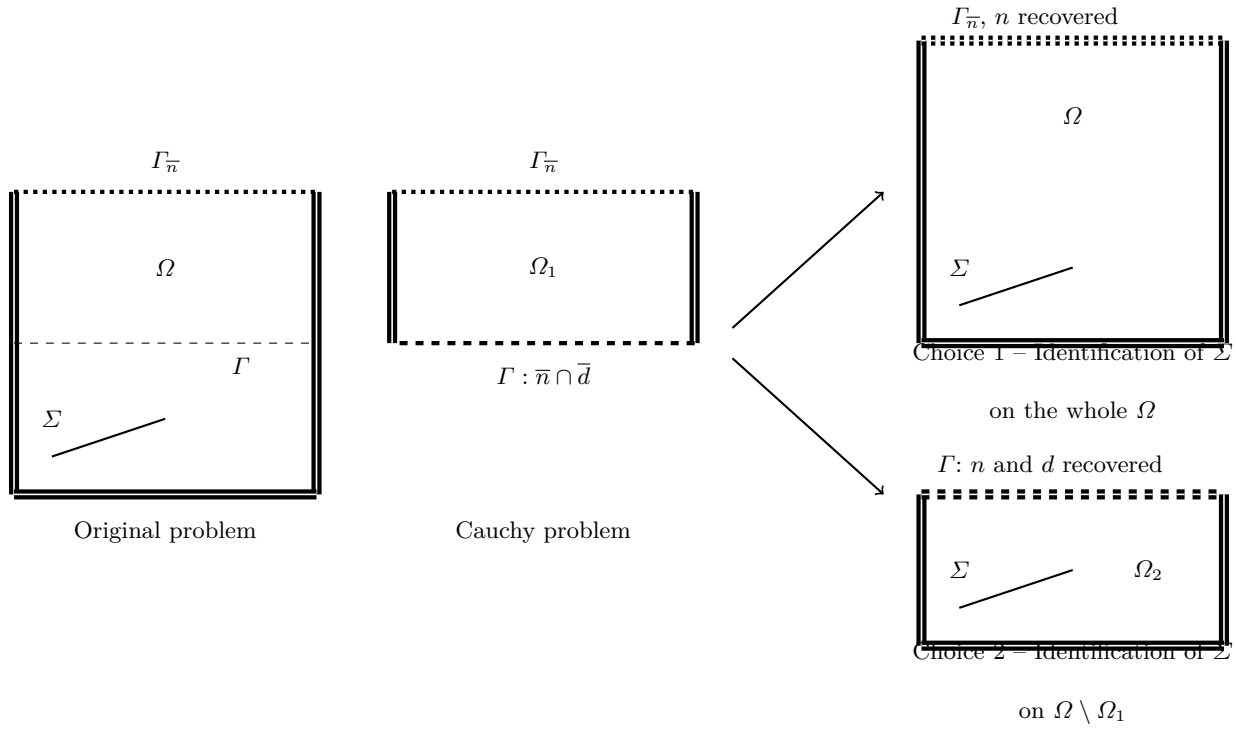

Fig. 4: Two ways to solve the crack identification problem with partial information (double bar means both Dirichlet and Neumann data are known)

3.2 Numerical study

In order to apply the proposed method, we suppose that the crack Σ is contained in the bottom-most half of the unit square. The first step consists in solving two Cauchy problems on the higher half of the square, Ω_1, corresponding to two of the four available load cases. All the combinations were tested and the couple $\{1, 3\}$ minimizes the distance between the two identified crack lines. In this numerical study, the mesh used for the direct computation is re-used for the resolution of the Cauchy problem, and its boundary elements are also used for the computation of the integrals needed for the reciprocity gap method. This "inverse problem crime" is deliberately committed in such a way to reveal the unreliability of the method. The mesh is constituted of 18142 triangle P1 elements with 8821 nodes, and the boundaries are refined. There are 500 elements on $\Gamma_{\overline{n}}$, 1500 on $\Gamma_n \cap \Gamma_d$ and 500 on Γ.

Figure 5 displays the relative errors on the identified $\underline{u}$ and $\underline{f}$ on the interface Γ. One can note that the error on $\underline{f}$ is, as usual for the Cauchy problem, much greater than the error on $\underline{u}$. What is more, the error on $\underline{f}$ dramatically increases when getting closer to the corners. Adding a smoothing step could be of interest, but this idea was not investigated in this study. Figure 6 presents the relative errors on the identification of $\underline{f}$ on the top side. One can remark that, as expected, the precision of the identification is much better on the top side $\Gamma_{\overline{n}}$ than on the interface Γ.

The crack identification procedure with polynomial reconstruction [19] is then either applied on the lower domain Ω_2 or on the full domain Ω. This proce-

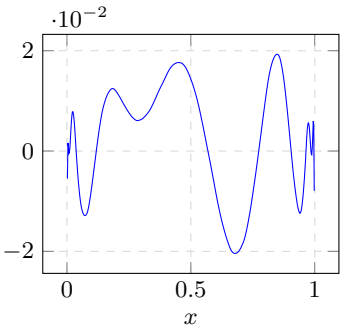

(a) Error on $u_{\Gamma,y}$

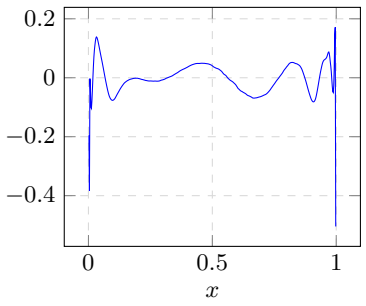

(b) Error on $f_{\Gamma,y}$

Fig. 5: Pointwise relative errors on u_y and f_y along Γ for load-case #1

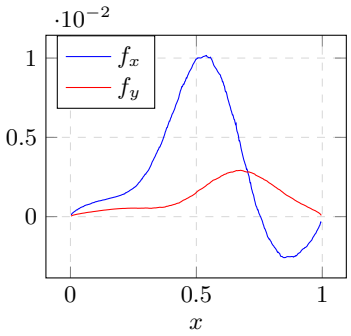

Fig. 6: Pointwise relative error on f_{top} for the load-case #1

dure permits to identify the line supporting the crack (2D version of Π, see the left part of Figures 7 and 8), and the displacement jump along this line. Using both test-cases 1 and 3 is only needed to identify the normal direction to the line. The precise location of the line along this normal can be computed from load-case 1 (green) or 3 (red). The reconstructed gap only uses the load-case 1 which is supposed to be the most favourable choice, see the right part of Figures 7 and 8.

Whatever the choice of domain, the identification of the crack's line is very satisfactory while the normal displacement jump suffers from the noise and its reconstruction has to be strongly regularized, making it very smooth. Anyway, this identification gives a correct idea of the position of the crack, but its length is impossible to deduce from the result.

3.3 Conclusion on the method

This method requires to know *a priori* that the crack is not in some part of the domain (Ω_1), that is sufficiently large to efficiently solve the Cauchy problem. What is more, in this method, the resolution of the

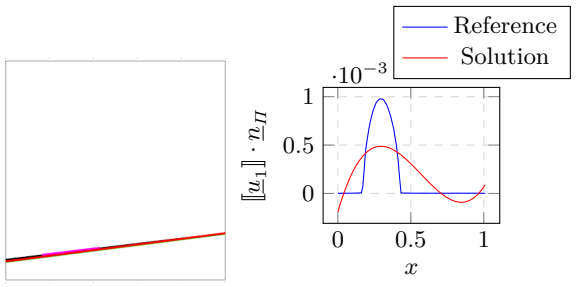

(a) Crack's line identification

(b) Identification of the normal displacement jump

Fig. 7: Identification of the crack, reconstruction on Ω_2 for the load-case 1

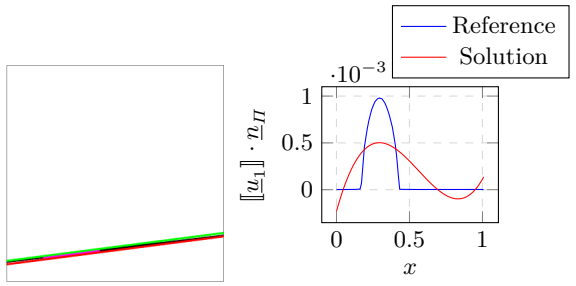

(a) Crack's line identification

(b) Identification of the normal displacement jump

Fig. 8: Identification of the crack, reconstruction on Ω for the load case 1

Cauchy problem has to be particularly precise in or-

der to provide the reciprocity gap algorithm with data of sufficient quality.

The stability of the crack identification problem is locally Lipschitz (at least in the case of straight emerging cracks, see [8, 10]), while the Cauchy problem, used as an intermediate step, is more severely ill-posed, with logarithmic stability and eigenvalues that tend to zero exponentially (see [13] for a spectral analysis or [1] for a stability analysis). As a consequence, this method is not optimal in term of stability. An other issue is that the Reciprocity Gap method presented in [7] can only be used with exactly 2 load cases. As a consequence, if more load cases are available (as in our example), this extra information can not be exploited. The last limitation of this approach is that it requires to solve two forward problems per iteration of the Steklov-Poincaré method in order to solve the Cauchy problem. This reduces the benefit from using the reciprocity gap method because the resolution of the Cauchy problem constitutes the computational bottleneck of the method.

On the other hand, the method can be straightforwardly applied on any geometry of the boundary, and for any kind of missing data (Dirichlet, Neumann or both).

4 Generation of adapted test-fields (PG0-RG method)

Let us consider the following subspace of admissible fields:

$$\mathcal{V}_0 = \left\{ \underline{v} \in \mathcal{V}, \quad \begin{array}{r} \underline{v} = 0 \text{ on } \Gamma_{\overline{d}} \\ \underline{\underline{\sigma}}(\underline{v}) \cdot \underline{n} = 0 \text{ on } \Gamma_{\overline{n}} \end{array} \right\} \tag{6}$$

We need to assume that $\Gamma_{\overline{d}} \cap \Gamma_{\overline{n}} = \emptyset$ in order for $\mathcal{V}_0$ not to be reduced to the null function. In words, the following method can not be applied to problems where a part of the boundary bears no information (neither Dirichlet nor Neumann). Under that hypothesis and assuming that the boundary is regular enough, it is possible to build fields in $\mathcal{V}_0$. For instance for piecewise polynomial boundary, one can use the method of [19]. However, in this case, a new condition emerges: $\Gamma_{\overline{d}}$ and $\Gamma_{\overline{n}}$ cannot exist on two different parts of the same polynomial-shaped surface. This is illustrated on Figure 9.

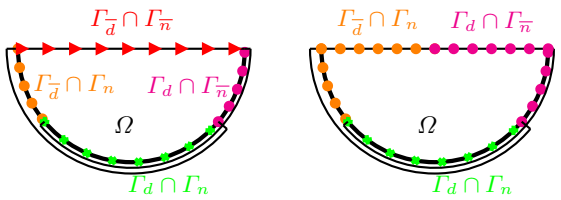

(a) $\mathcal{V}_0 = \emptyset$

(b) $\mathcal{V}_0$ does not contain any polynomial

Fig. 9: Two cases where polynomials test-functions cannot be build

The advantage of using test fields in $\mathcal{V}_0$ is that the boundary integral of (2) can be evaluated without

difficulty because the terms on $\Gamma_{\overline{d}}$ and $\Gamma_{\overline{n}}$ vanish:

$$\begin{aligned} &\forall \underline{v} \in \mathcal{V}_0, \forall r \in [\![1; r_{\max}]\!], \\ \mathrm{RG}_r(\underline{v}) &= \int_{\partial\Omega} (\underline{f}_r \cdot \underline{v} - \underline{u}_r \cdot \underline{\underline{\sigma}}(\underline{v}) \cdot \underline{n}) \,\mathrm{dS} \\ &= \int_{\Gamma_n} \widehat{\underline{f}}_r \cdot \underline{v} \,\mathrm{dS} - \int_{\Gamma_d} \widehat{\underline{u}}_r \cdot \underline{\underline{\sigma}}(\underline{v}) \cdot \underline{n} \,\mathrm{dS} \end{aligned} \tag{7}$$

On the numerical point of view, the determination of a basis of a finite-dimensional subset of $\mathcal{V}_0$ can be done thanks to the kernel of the discrete form of the operator $\mathrm{div}(\underline{\underline{\sigma}}(\bullet))$, combined with boundary conditions. This operation can be realized once for all for a given constitutive law. In practice, in our implementation, this computation appears not to be costly.

Anyhow, as said earlier, the test fields that permit to compute the coordinates of the Plane Π, as proposed in [7], do not belong to $\mathcal{V}_0$. We thus propose a technique that identifies simultaneously the plane Π and the displacement jump (whose support represents the crack Σ).

4.1 Principle of the method

We introduce $e_r(\Pi, \underline{u}_j, \underline{v})$, the identification error between the values given by (2) and (4) for a load case r, a plane Π, a displacement jump $\underline{u}_j$ and a test-function $\underline{v}$ in $\mathcal{V}_0$.

$$\begin{aligned} e_r(\Pi, \underline{u}_j, \underline{v}) &= \int_{\Pi} \underline{\underline{\sigma}}(\underline{v}) : (\underline{n}_\Pi \otimes \underline{u}_j) \,\mathrm{dS} \\ &- \left(\int_{\Gamma_n} \widehat{\underline{f}}_r \cdot \underline{v} \,\mathrm{dS} - \int_{\Gamma_d} \widehat{\underline{u}}_r \cdot \underline{\underline{\sigma}}(\underline{v}) \cdot \underline{n} \,\mathrm{dS} \right) \end{aligned} \tag{8}$$

Proposition 1 *If Π is the actual crack plane, and if $[\![\underline{u}_r]\!]$ is the actual displacement jump for the load-case r, $e_r(\Pi, [\![\underline{u}_r]\!], \underline{v})$ vanishes for any $\underline{v}$ in $\mathcal{V}_0$.*

Proof The proof follows from the application of equation (3) in the definition of $e_r(\Pi, [\![\underline{u}_r]\!], \underline{v})$.

In [10], the identifiability of cracks from one measurement is demonstrated in the case where the displacement is not smooth at the vicinity of the crack tips, and in the 2D framework. However, the utilization of more than one test cases is expected to increase the stability of the resolution. That is why we propose to minimize, in the mean square sense, the errors $(e_r(\Pi, [\![\underline{u}_r]\!], \underline{v}))$, for r_{max} different load cases and n different test-functions $\left(\underline{\psi}_i\right)_{i=1\ldots n}$ in $\mathcal{V}_0$. Let us introduce the minimization problem over Π in the set of planes of $\mathbb{R}^d$, and over $[\![\underline{u}_r]\!]$ in $H^{1/2}(\omega)$:

$$\min_{\Pi, ([\![\underline{u}_r]\!])_r} \frac{1}{2} \sum_{r=1}^{r_{\max}} \sum_{i=1}^{n} \left(e_r(\Pi, [\![\underline{u}_r]\!], \underline{\psi}_i) \right)^2 \tag{9}$$

In practice, the plane Π can be characterized by few parameters (2 in 2D, 3 in 3D) which we gather in the vector θ. To emphasize this, the plane is now denoted by Π_θ. As said earlier non-flat surface could be considered, it would just make the number of parameters and the computational cost higher.

Regarding $[\![\underline{u}_r]\!]$, it is sought in a subspace of $H^{1/2}(\omega_\theta)$ of dimension m spanned by finite element shape functions $(\phi_{\theta,j})_{j=1\ldots m}$, and we define the vectors of the corresponding amplitudes: $\alpha_\theta^r = \left(\alpha_{\theta,j}^r\right)_{j=1\ldots m}$. The minimization problem can then be written as:

$$\min_{\theta, (\alpha_\theta^r)_r} \frac{1}{2} \sum_{r=1}^{r_{\max}} \sum_{i=1}^{n} \left(e_r(\Pi_\theta, \sum_{j=1}^{m} \alpha_{\theta,j}^r \phi_{\theta,j}, \underline{\psi}_i) \right)^2 \tag{10}$$

Remark 1 *The vector θ could be appended with other unknown parameters to be identified (material coefficients, geometrical details).*

Problem (10) is exactly the minimization problem that results from the Petrov-Galerkin projection of the equations (2) and (4) for each r in range $[\![1; r_{\max}]\!]$. It can then be algebraically rewritten:

$$\min_{\theta,(\alpha_\theta^r)_r} \frac{1}{2} \sum_{r=1}^{r_{\max}} \|A_\theta \alpha_\theta^r - b^r\|_2^2 \tag{11}$$

With the following notations:

$$\begin{aligned} b_i^r &= \int_{\Gamma_n} \underline{\widehat{f}}_r \cdot \underline{\psi}_i \,\mathrm{dS} - \int_{\Gamma_d} \underline{\widehat{u}}_r \cdot \underline{\underline{\sigma}}(\underline{\psi}_i) \cdot \underline{n} \,\mathrm{dS} \\ A_{\theta,ij} &= \int_{\omega_\theta} \underline{\underline{\sigma}}(\underline{\psi}_i) : (\underline{n}_{\Pi_\theta} \otimes \phi_{\theta,j}) \,\mathrm{dS} \end{aligned} \tag{12}$$

Remark 2 *The method finds the crack's parameters, and displacement gap that minimize the reciprocity gap. As such, it can be linked to the more-conventional PDE-constrained minimization methods, that consist in minimizing a well-chosen cost-function under the constraint of respecting the PDE. These methods applied to parameter identification are detailed for example in [9]. In the case of our algorithm, the PDE constraint is enforced via the choice of the test-functions in $\mathcal{V}_0$, which ensures that one does not have to iteratively solve the direct problem, in the same vein as the reciprocity likelihood minimization method [3].*

As this minimization problem is very likely to be unstable due to the inherent ill-posedness of the problem (Appendix A provides some elements to understand the properties of Matrix A), we add a quadratic symmetric semi-definite positive regularization term $\alpha_\theta^{rT} M_\theta^T M_\theta \alpha_\theta^r$ to the functional. The weight of that term is tuned by the positive real parameter μ:

$$\min_{\theta,(\alpha_\theta^r)_r} \frac{1}{2} \sum_{r=1}^{r_{\max}} \|A_\theta \alpha_\theta^r - b^r\|_2^2 + \frac{\mu}{2} \|M_\theta \alpha_\theta^r\|_2^2 \tag{13}$$

In practice, we propose M_θ to stand for the "Frobenius norm of the surface gradient" operator:

$$\|M_\theta \alpha_\theta^r\|_2^2 = \int_{\omega_\theta} \|\nabla [\![\underline{u}_r]\!]\|_F^2 \mathrm{dS} \tag{14}$$

The kernel of $M_\theta^T M_\theta$ is spanned by constant fields, this does not affect the regularization since the instability only affects oscillatory terms.

In the end, the cost-functional to be minimized can be written as:

$$\begin{aligned} &\Upsilon(\theta, (\alpha_\theta^r)_r) = \\ &\frac{1}{2} \sum_{r=1}^{r_{\max}} \left(\alpha_\theta^{rT} \left(A_\theta^T A_\theta + \mu M_\theta^T M_\theta \right) \alpha_\theta^r - \alpha_\theta^{rT} A_\theta^T b^r \right) \end{aligned} \tag{15}$$

As it naturally arises, the minimization of Υ is conducted in a nested way: the inner loop seeks (α_θ^r) for a given θ, while the outer loop seeks the optimal θ. We introduce the following notations:

$$\tilde{\alpha}_\theta^r = \underset{(\alpha_\theta^r)_r}{\arg\min}\, \Upsilon(\theta, (\alpha_\theta^r)_r) \tag{16}$$

$$\Phi(\theta) = \Upsilon(\theta, (\tilde{\alpha}_\theta^r)_r) \tag{17}$$

4.2 Technical choices

$(\underline{\psi}_i)_{i=1\ldots n}$ is chosen to be a basis of $\mathcal{V}_0 \cap \mathbb{R}_{20}[x, y, z]$, the vector subspace of admissible polynomials with degree less or equal to 20. The construction of such a basis is described in [19].

$(\phi_{\theta,j})_{j=1\ldots m}$ is the basis of finite element shape functions associated to a 2D mesh of the surface ω_θ. These functions have local support, contrary to

the functions commonly used with the reciprocity gap method [7,4]. This is made possible by the Petrov-Galerkin procedure and has several advantages. Firstly, as the crack is supposed to occupy only a small part of the surface ω_θ, it better renders the local variations of the displacement jump function. Secondly, it permits refining locally some parts of the mesh. Finally, regularization is easy to apply in this framework.

In practice, the mesh is made out of triangles, and first degree shape functions are used. For any position θ of the plane Π_θ, one has to mesh $\omega_\theta = \Pi_\theta \cap \Omega$ in order to compute the matrices A_θ and M_θ. The resulting mesh is denoted by $\mathfrak{M}_\theta$. While in the 2D case the crack is 1D and meshing is trivial, in the 3D case the meshes were generated with Gmsh software [20]. In practice, this mesh generation is sufficiently efficient to have only a negligible impact on the overall computational cost of the algorithm

The quality of the solution can be improved by some a priori knowledge:

- If the crack is known not to be emerging, then all the boundary degrees of freedom of $\partial\omega_\theta$ can be imposed null Dirichlet conditions. If T_θ is the discrete trace operator, this condition can be written as $T_\theta \alpha_\theta^r = 0$.
- Since there is no interpenetration, we know that $[\![\underline{u}_r]\!]\cdot\underline{n}_{\Pi_\theta} \geqslant 0$. If C_θ is (the opposite of) the discrete counterpart to the normal projection on the crack plane, this condition can be written as $C_\theta \alpha_\theta^r \leqslant 0$.

Finally, the minimization can be written as:

$$\min_{\theta,\left(T_\theta \alpha_\theta^r = 0, C_\theta \alpha_\theta^r \leqslant 0\right)_r} \Upsilon(\theta, (\alpha_\theta^r)_r) \tag{18}$$

Where Υ is defined in equation (15). In this context, the minimization with respect to (α_θ^r) for a given θ can be run with an Uzawa algorithm.

Choosing θ in order to configure the plane Π_θ is not a trivial question, since the set of planes (aka projective space) is not a vector space. Moreover, in order to help the outer minimization, it is of interest to use coordinates which makes $\omega_\theta = \Pi_\theta \cap \Omega$ a smooth function of θ. We only proposed ad hoc solutions, leaving room to future improvement. In the 2D case of Figure 3, the line Π is located by its intersections with the boundary of Ω, themselves identified by two angles from the centroid and x axis (see Figure 10). This kind of positioning should extend to any star-shaped domain.

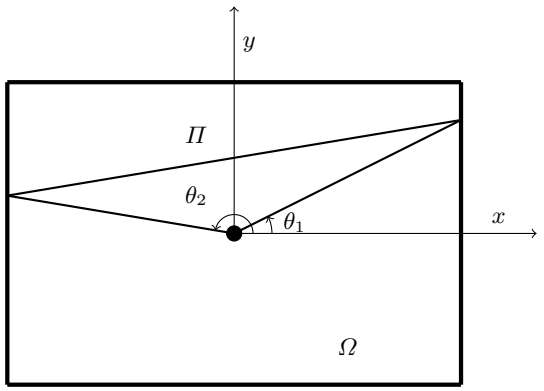

Fig. 10: Parameters θ_1 and θ_2 that define the crack's "plane" in 2D

In the 3D case, we chose to work with the equation of Π: $\theta_0 + \theta_1 x + \theta_2 y + \theta_3 z = 0$ with $\|\theta\|_2 = 1$. This kind of configuration makes it a little more tricky to

bound the domain of search (where $\omega_\theta \neq \emptyset$) and to ensure smooth variations of Φ.

The outer minimization (with respect to θ), is performed via a Newton algorithm that finds the roots of the gradient of $\Phi(\theta)$. This gradient is estimated with finite differences, and the Hessian is approximated via the sensibility matrices. Algorithm 1 presents the method. It calls for a series of remarks.

- The choice of the sampling step p_s of the finite difference evaluation of the gradient is important: for too large p_s, the error on the identified parameters stagnates quickly while, for too small p_s, the algorithm may not be able to efficiently optimize the parameters, mostly because of round-off effect. For that reason, it was chosen to adapt p_s to the evolution of the parameters by writing $p_s = \min(k\frac{\delta\theta_s}{\theta_s}, p_{\min})$, with $k = O(10^{-1})$ (variations of k have little effect around this value), and $p_{\min}$ the minimal step.
- This algorithm makes use of a positive parameter, denoted by k_u and a sufficient condition for the convergence of the algorithm is that $k_u < \min(\text{eig}(A_\theta^T A_\theta + \mu M_\theta^T M_\theta))$ (provided each line of C_θ has norm 1). Thus, a possibility is to use for k_u an estimation of the smallest non-zero eigenvalue of the regularization operator $(\mu M_\theta^T M_\theta)$.

  In our implementation, the Uzawa algorithm performed a fixed number of iterations, namely 100. A straightforward improvement would be to use a variable criterion on the stagnation of $\langle C_\theta \alpha^r \rangle^+$ which should decrease when θ converges. This would make it possible to avoid long computations for the first steps for which the identified displacement jump is anyway quite wrong.
- In practice, the minimization problems that have to be solved under inequality constraint for the different load-cases r share the same left-hand side. As a consequence, a multiple right-hand side strategy can be used during the Uzawa algorithm.
- The test-functions being high order polynomials, they are expected to be very oscillatory, and thus to amplify the noise present on the fields with which they are multiplied, and to cause high integration errors. This phenomenon is the numerical consequence of the ill-posedness of the inverse problem, and is remedied by the regularization term.
- The computation of the integrals on the boundary that appear in the definition of the reciprocity gap functional, and in the terms of the matrix A are done by Gaussian integration on a mesh of the surface with 2 Gauss points on edges (2D case) and 3 Gauss points on triangles (3D case). We checked that using more Gauss points did change only marginally the numerical values of the right and left hand sides, and did not improve the quality of the result.
- In the finite difference approximation, we need to compare quantities, like the gradient $M_\theta \tilde{\alpha}_\theta$, defined on different meshes $\mathfrak{M}_{\theta+d\theta}$ and $\mathfrak{M}_\theta$. This was conducted by mesh projection, which is a costly

Algorithm 1: Nested optimizations algorithm with adapted test-functions

μ and k given parameters, initialization θ_0 and p_0 given;

for $s = 0, 1, \ldots, n$ *(convergence)* **do**

Re-mesh the surface and assemble A_{θ_s}, M_{θ_s} and $C(\theta_s)$;

for $r = 1, 2, \ldots, r_{\max}$ *(load cases)* **do**

Find (using Uzawa algorithm): $\tilde{\alpha}^r_{\theta_s} = \underset{\left(T_{\theta_s}\alpha^r_{\theta_s}=0, C_{\theta_s}\alpha^r_{\theta_s}\leqslant 0\right)_r}{\arg\min} \Upsilon(\theta_s, (\alpha^r_{\theta_s})_r)$

Find a basis $\{e_1, \ldots, e_d\}$ of $\theta_s^\perp$, of dimension $d = 2$ or 3;

for $j = 1, 2, \ldots, d$ **do**

Set $\theta_{s,j} = \theta_s + p_s e_j$, re-mesh the surface to assemble $A_{\theta_{s,j}}$ and $M_{\theta_{s,j}}$;

for $r = 1, 2, \ldots, r_{\max}$ *(the load cases)* **do**

Find (using Uzawa algorithm): $\tilde{\alpha}^r_{\theta_{s,j}} = \underset{\left(T_{\theta_{s,j}}\alpha^r_{\theta_{s,j}}=0, C_{\theta_{s,j}}\alpha^r_{\theta_{s,j}}\leqslant 0\right)_r}{\arg\min} \Upsilon(\theta_{s,j}, \left(\alpha^r_{\theta_{s,j}}\right)_r)$

for $r = 1, 2, \ldots, r_{\max}$ *(the load cases)* **do**

$\mathcal{A}_r = \frac{1}{p_s}\left(\ldots A_{\theta_{s,j}}\tilde{\alpha}^r_{\theta_{s,j}} - A_{\theta_s}\tilde{\alpha}^r_{\theta_s} \ldots\right)$ and $\mathcal{M}_r = \frac{1}{p_s}\left(\ldots M_{\theta_{s,j}}\tilde{\alpha}^r_{\theta_{s,j}} - M_{\theta_s}\tilde{\alpha}^r_{\theta_s} \ldots\right)$;

$g = \sum_{r=1}^{r_{\max}}\left(\mathcal{A}_r^T(A_{\theta_s}\tilde{\alpha}^r_{\theta_s} - b^r) + \mu\mathcal{M}_r^T M_{\theta_s}\tilde{\alpha}^r_{\theta_s}\right)$ approximation of $\nabla\Upsilon_s$;

$H = \sum_{r=1}^{r_{\max}}\left(\mathcal{A}_r^T\mathcal{A}_r + \mu\mathcal{M}_r^T\mathcal{M}_r\right)$ approximation of $\nabla^2\Upsilon_s$;

$\delta\theta_s = -H^{-1}g, \qquad \theta_{s+1} = \theta_s + \delta\theta_s, \qquad p_s = k\frac{\|\delta\theta_s\|}{\|\theta_s\|}$;

operation. Using mesh morphing instead led to similar overall behavior of the algorithm.

– In some cases, it was observed that the proposed algorithm stagnated around sub-optimal solutions. We investigated using BFGS for the outer minimization. This quasi-Newton method has the advantage not to require mesh projection for the update of the matrices, but it did not lead to much improved solutions.

We also tested using Markov chains. This method does not need to compute gradient nor Hessian, and statistically leads to safer convergence.

However, the convergence rate was drastically decreased, making it less convenient than the Newton method presented above which was used in all the following examples.

4.3 Numerical study

We evaluate the method on the 2D test-case of Figure 3 where the space of test functions only needs to be adapted to the missing Neumann data on the top side. For this numerical study, it was chosen to interpolate the measurement on a coarse mesh that is different from the mesh used for the direct computation. By this means, even when no synthetic noise is explicitly added, the measured data are slightly incompatible.

In a first time, we propose on Figure 11 a map of the cost-function Φ with respect to (θ_1, θ_2). Note

that each evaluation of the cost-function requires one minimization with respect to $(\alpha_\theta^r)_r$.

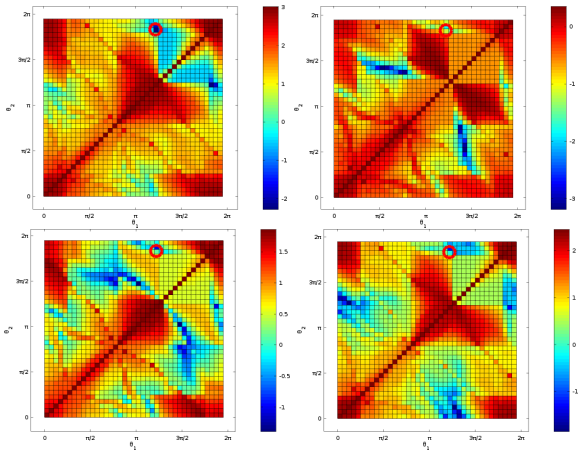

Fig. 11: Cost-function logarithm map for different load-cases (The red circle is centred on the reference value)

The first remark about those maps is that the cost-function is symmetric with respect to the second diagonal, because θ_1 and θ_2 are interchangeable. Also, as the parameters are angles, the space is 2π periodic. Clearly, the functions are not convex, and they do not necessarily have a unique minimum. Moreover, the functions do not strictly vanish for the reference value, because of at least three factors. First, even if no synthetic noise was added, the data comes from an approximate solution. Second, a transfer was necessary between the finite element mesh to the surface mesh used for the computation of integrals. Finally, the cost-function is only evaluated for discrete values of (θ_1, θ_2).

Table 1 presents the Euclidean norm the right-hand side (RHS) of the linear system associated to each load case. This norm is proportional to the magnitude of the displacement jump along the crack, which means that the load-cases with the largest right-hand side norm have also the most favourable signal-to-noise ratio. This information can be used to determine which load case is the most suited for the identification. In our example, the first load-case leads to the largest RHS, and on Figure 11, the map resulting from it is the one with the sharpest minimum. What is more, the argument of this minimum is very close to the reference value. Loads 1 and 4 open the crack more than loads 2 and 3, and lead to a higher norm of the corresponding right hand side and to a lower relative error on the displacement jump.

As nothing ensures that the load cases actually open the crack, the information of the norm of this RHS can be used to distinguish load cases that lead to a gap having a reasonable amplitude from the others.

In order to validate numerically the relevance of Tikhonov regularization, we estimate the condition number of the system at θ's reference value, for different values of the regularization parameter, see Figure 12a. One can observe as well on Figure 12b, that the condition number is practically not impacted by the number of degrees of freedom of the chosen discretization and the degree of the polynomial test-functions.

In order to tune the regularization, we propose to use the L-curve method (see Figure 13). Below a given value of μ, close to 10, non-physical oscillations of the displacement jump field appear, which make the norm of the gradient of the displacement jump explode. For

Load case	1	2	3	4
RHS Euclidean norm	32.427	1.5031	8.5605	16.827
Relative error on the displacement jump identification	0.10775	1.3757	1.0282	0.40753

Table 1: Amplitude of the different right hand sides and associated error

numerical examples made on the test-cases of Figure 11, both with method PG0-RG and gPG-RG, this value $\mu = 10$ is used, unless otherwise stated.

The parameters θ_1 and θ_2 (see Figure 10) were initialized by: $\theta_1^0 = 0$ and $\theta_2^0 = \pi$. This corresponds to a horizontal line of equation $y = 1/2$. The decrease of the cost-function with the iterations is displayed on Figure 14.

The identification of the crack's line is presented on Figure 15, it is very close to the reference line used for the direct computation. On Figure 17, the identified displacement jump over this line is compared to the true displacement jump over the reference line for the different load cases. It is noteworthy that the more the load opens the crack, the larger is the right-hand side and the more precise is the identification (as seen on Table 1).

Remark 3 *The reference (forward) computation was conducted on a mesh with an explicit crack (double nodes). The displacement jump is measured as the difference between the displacements on two close lines located on both sides of Π. As a consequence, the value of the reference displacement jump does not exactly vanish outside the crack.*

Remark 4 *In the case where the applied load does not open the crack, it is necessary to study the tangential components of the displacement jump, that are available by the proposed method, but not displayed here. However, for the seek of stability, it is much preferable that at least one load-case leads to a non-vanishing normal gap.*

4.4 Conclusion on the PG0-RG method

This method is limited by the need to construct test-functions that are in $\mathcal{V}_0$. In our case of polynomial test-functions, it is feasible to design such functions for (piecewise) polynomial boundaries with Dirichlet or Neumann missing data. But, if the data is missing only on a small part of a line, this method leads to ignoring the data on the entire line.

On the other hand, and contrarily to the previously-presented C-RG method, it is not necessary to assume that the crack is contained in a part of Ω. The comparison of the results of figures 8 and 17 show that this method can also achieve a better accuracy since for the C-RG method the noise on Cauchy data induces a stronger noise on the data used in the reciprocity gap step. As the used test-functions respect the equilibrium by themselves, the method does

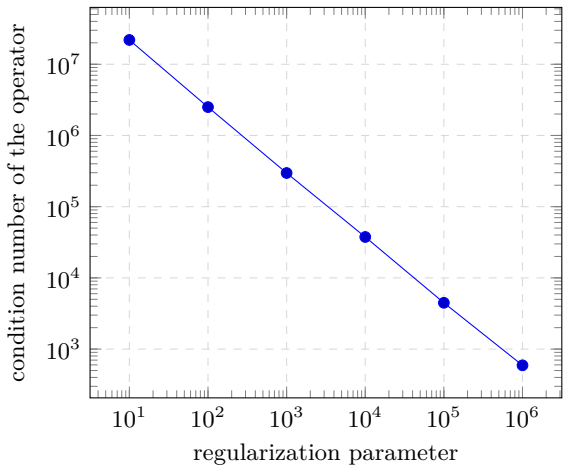

(a) Condition number of the operator w.r.t. regularization parameter μ for 50 dofs and test-polynomials of order 20

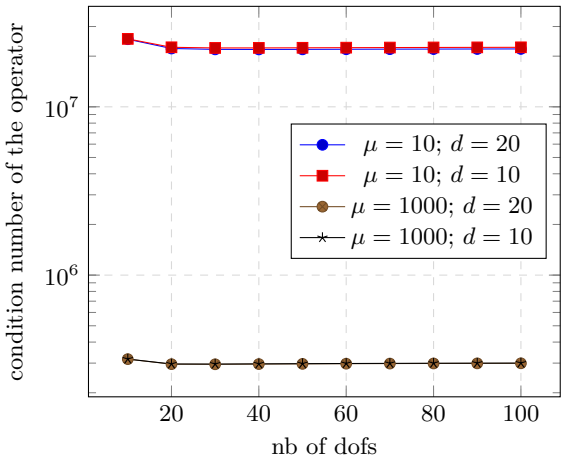

(b) Condition number of the operator w.r.t. number of dofs for different regularization μ and degree d of test-polynomials

Fig. 12: Influence of the parameters of the computation on the condition number

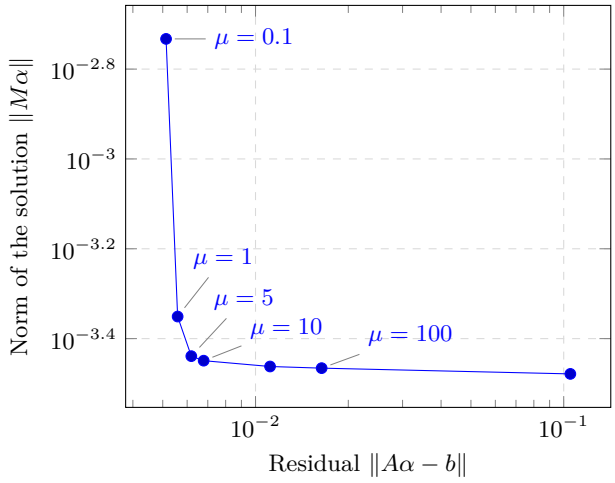

Fig. 13: L-curve for polynomials of degree 20, with 50 dof on the crack – PG0-RG method (Section 4).

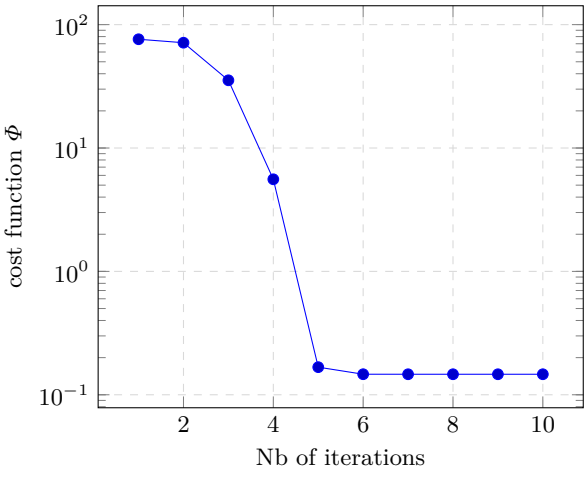

Fig. 14: Convergence of the outer minimization – PG0-RG method (Section 4).

not require to solve any direct problem, which means that most of the benefit of the reciprocity gap method remains. Anyhow, there is a significant cost in computing, at each iteration, the small matrices A_θ (which is moreover dense) and M_θ.

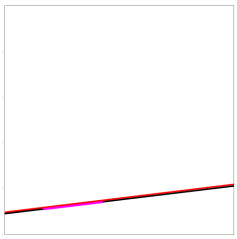

Fig. 15: Identification of the crack's line – PG0-RG method (Section 4)

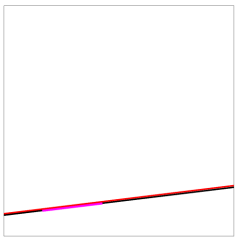

Fig. 16: Identification of the crack's line – gPG-RG method (Section 5)

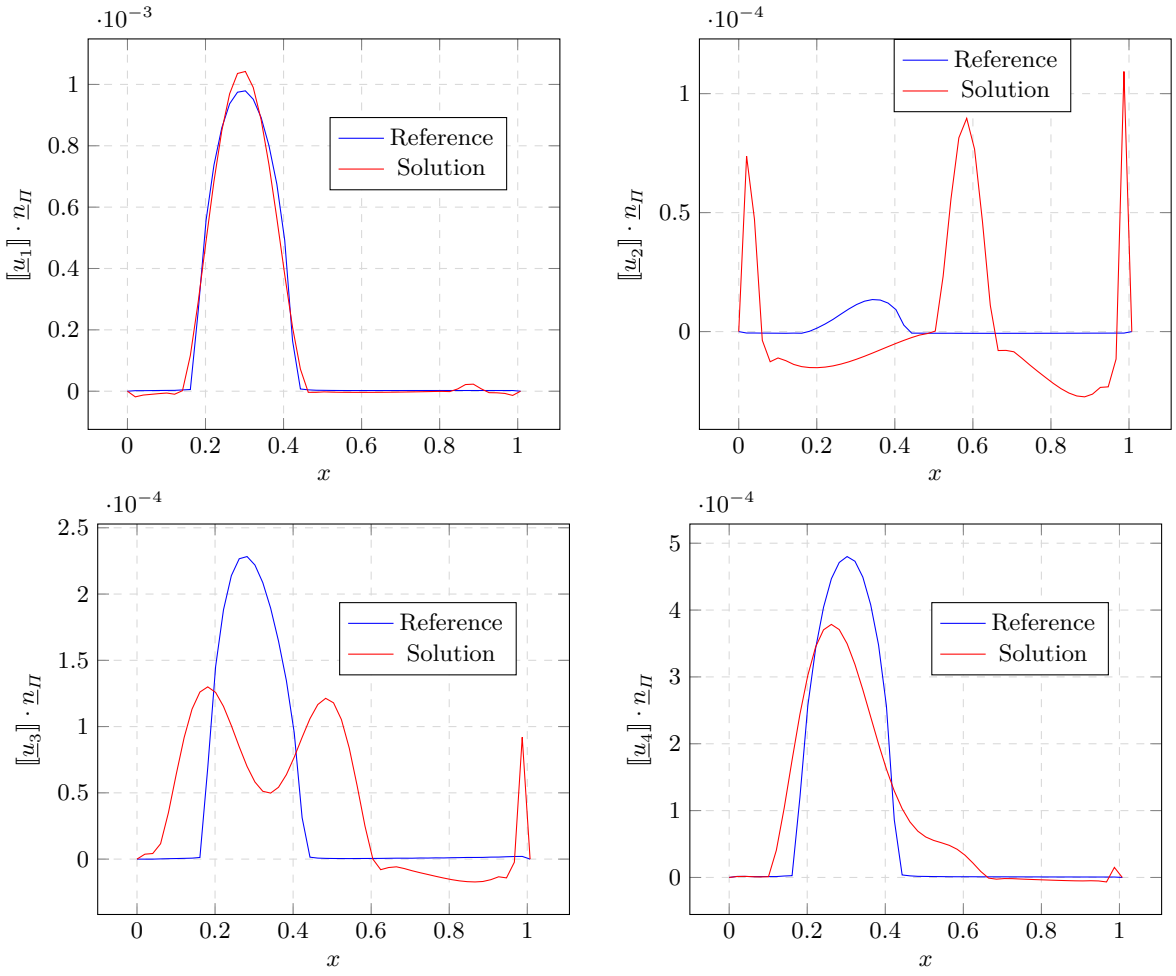

Fig. 17: Identification of the normal displacement jump – PG0-RG method (Section 4)

5 Simultaneous search of missing boundary conditions (gPG-RG method)

This approach is technically close to the PG0-RG method but instead of trying to eliminate the unknown boundary conditions by constructing the space $\mathcal{V}_0$, we use test-functions in $\mathcal{V}$ (ie. that only respect the local equilibrium inside the domain), and we try to identify the boundary conditions together with the crack.

5.1 Presentation of the method

Let us rewrite the definition of the reciprocity gap functional (2), and separate the integrals on the different parts of the boundary. We distinguish the known part of the force $\underline{\widehat{f}}_r$, defined on Γ_n, from the unknown part of the force $\underline{\widetilde{f}}_r$, defined on $\Gamma_{\bar{n}}$. The same distinction is made on the boundary displacement: on Γ_d, $\underline{\widehat{u}}$ is known, whereas on $\Gamma_{\bar{d}}$, $\underline{\widetilde{u}}$ is unknown. Note that $\underline{\widehat{u}}$ and $\underline{\widetilde{u}}$ are tied by the $H^{1/2}(\partial\Omega)$ continuity at $\bar{\Gamma}_d \cap \bar{\Gamma}_{\bar{d}}$. For simplicity reasons, we assume that $\underline{\widehat{u}}$ is 0 on $\partial\Gamma_d$, so that $\underline{\widetilde{u}}$ should be sought in $H_{00}^{1/2}(\Gamma_{\bar{d}})$.

Similarly as in (8), we introduce $\check{e}_r(\Pi, \underline{u}_j, \underline{\widetilde{f}}, \underline{\widetilde{u}}, \underline{v})$, the difference between the values given by (2) and (4) for a load case r, a plane Π, a displacement jump $\underline{u}_j$, force $\underline{\widetilde{f}}$ on $\Gamma_{\bar{n}}$, displacement $\underline{\widetilde{u}}$ on $\Gamma_{\bar{d}}$ and a test-function $\underline{v}$ in $\mathcal{V}$.

$$\begin{aligned}\check{e}_r(\Pi, \underline{u}_j, \underline{\widetilde{f}}, \underline{\widetilde{u}}, \underline{v}) = &\int_\Pi \underline{\underline{\sigma}}(\underline{v}) : (\underline{n}_\Pi \otimes \underline{u}_j)\,\mathrm{dS} \\ &- \left(\int_{\Gamma_{\bar{n}}} \underline{\widetilde{f}} \cdot \underline{v}\,\mathrm{dS} - \int_{\Gamma_{\bar{d}}} \underline{\widetilde{u}} \cdot \underline{\underline{\sigma}}(\underline{v}) \cdot \underline{n}\,\mathrm{dS}\right) \\ &- \left(\int_{\Gamma_n} \underline{\widehat{f}}_r \cdot \underline{v}\,\mathrm{dS} - \int_{\Gamma_d} \underline{\widehat{u}}_r \cdot \underline{\underline{\sigma}}(\underline{v}) \cdot \underline{n}\,\mathrm{dS}\right) \quad (19)\end{aligned}$$

This identification error vanishes for the right crack plane Π, the right displacement jump $[\![\underline{u}_r]\!]$ and the right forces and displacement $\underline{\widetilde{f}}_r$ and $\underline{\widetilde{u}}_r$ on $\Gamma_{\bar{n}}$ and $\Gamma_{\bar{d}}$. As in (9), we introduce n different test-functions $(\underline{\psi}_i)_{i=1\dots n}$ in $\mathcal{V}$, and we write the following minimization problem :

$$\min_{\Pi, \left([\![\underline{u}_r]\!], \underline{\widetilde{u}}_r, \underline{\widetilde{f}}_r\right)_r} \frac{1}{2} \sum_{r=1}^{r_{\max}} \sum_{i=1}^{n} \left(\check{e}_r(\Pi, [\![\underline{u}_r]\!], \underline{\psi}_i, \underline{\widetilde{f}}_r, \underline{\widetilde{u}}_r)\right)^2 \quad (20)$$

As previously, we introduce the family $(\phi_{\theta,j})_{j=1\dots m}$, that spans the space describing $[\![\underline{u}_r]\!]$. Two other families have to be introduced as well. The approximation of $\underline{\widetilde{f}}_r$ lives in the space spanned by $(\chi_k)_{k=1\dots p}$, of dimension p, and the approximation of $\underline{\widetilde{u}}_r$ lives in the space spanned by $(\rho_l)_{l=1\dots q}$, of dimension q. The corresponding amplitude vectors are respectively $\alpha_\theta^r = \left(\alpha_{\theta,j}^r\right)_{j=1\dots m}$, $\beta^r = (\beta_k^r)_{k=1\dots p}$ and $\gamma^r = (\gamma_l^r)_{l=1\dots q}$. The minimization problem then reads:

$$\min_{\theta, \left(\alpha_\theta^r, \beta^r, \gamma^r\right)_r} \frac{1}{2} \sum_{r=1}^{r_{\max}} \sum_{i=1}^{n} \left(\check{e}_r\left(\Pi, \sum_{j=1}^{m} \alpha_{\theta,j}^r \phi_{\theta,j}, \underline{\psi}_i, \sum_{k=1}^{p} \beta_k^r \chi_k, \sum_{l=1}^{q} \rho_l \gamma_l^r\right)\right)^2 \quad (21)$$

As previously, this problem can be algebraically written as:

$$\min_{\theta, \left(\alpha_\theta^r, \beta^r, \gamma^r\right)_r} \frac{1}{2} \sum_{r=1}^{r_{\max}} \|\Phi_\theta \alpha_\theta^r + X\beta^r + R\gamma^r - b^r\|^2 \quad (22)$$

with:

$$\begin{aligned} b_i^r &= \int_{\Gamma_n} \widehat{\underline{f}}_r \cdot \underline{\psi}_i \,\mathrm{dS} - \int_{\Gamma_d} \widehat{\underline{u}}_r \cdot \underline{\underline{\sigma}}(\underline{\psi}_i) \cdot \underline{n} \,\mathrm{dS} \\ \Phi_{\theta,ij} &= \int_{\omega_\theta} \underline{\underline{\sigma}}(\underline{\psi}_i) : (\underline{n}_{\Pi_\theta} \otimes \phi_{\theta,j}) \,\mathrm{dS} \\ X_{ik} &= -\int_{\Gamma_{\bar{n}}} \chi_k \cdot \underline{\psi}_i \,\mathrm{dS} \\ R_{il} &= \int_{\Gamma_{\bar{d}}} \rho_l \cdot \underline{\underline{\sigma}}(\underline{\psi}_i) \cdot \underline{n} \,\mathrm{dS} \end{aligned} \tag{23}$$

The assembly of the matrices X and R, is one of the most costly steps, because they are fully populated. Fortunately, this operation can be done once for all. Φ_θ is dense as well, and while its size is much smaller, its assembly has to be done at each iteration as it depends on the position of the plane Π_θ, making it a potential bottleneck for the method.

The minimization is regularized by two terms which respectively penalize the L_2 norm of $\widetilde{\underline{f}}_r$ and the gradients of $\widetilde{\underline{u}}_r$ and $[\![u_r]\!]$ as in equation (14). Thus, the discrete operators M_θ, M_X and M_R are introduced in order to build the desired quantities from the degrees of freedom. The sparse structure of these matrices ensures that the numerical cost of their assembly remains small.

$$\begin{aligned} \min_{\theta,(\alpha_\theta^r,\beta^r,\gamma^r)_r} \frac{1}{2} \sum_{r=1}^{r_{\max}} \Bigg(& \|A_\theta \alpha_\theta^r + X\beta^r + R\gamma^r - b^r\|^2 \\ & + \frac{\mu}{2}\|M_\theta \alpha_\theta^r\|_2^2 + \frac{\mu}{2}\eta\|M_X\beta^r\|_2^2 + \frac{\mu}{2}\|M_R\gamma^r\|_2^2 \Bigg) \end{aligned} \tag{24}$$

Remark 5 (Regularization of the boundary displacement) *At that point, it is crucial to take into account the continuity of $\widetilde{\underline{u}}_r$ during the regularization. In other words, the regularization acts on the displacement fields on $\bar{\Gamma}_{\bar{d}}$ with known values on $\partial\Gamma_{\bar{d}}$. In particular, if $\widehat{\underline{u}}_r$ was non-zero on $\partial\Gamma_{\bar{d}} \cap \partial\Gamma_d$, the regularization would contribute to the right-hand side of the problem. Note that this remark extends to point-wise measurements in a discrete setting. For the sake of simplicity, we assume the displacement is known to be zero on $\partial\Gamma_{\bar{d}}$.*

We introduce the following notations:

$$\begin{aligned} \mathbf{A}_\theta &= \begin{pmatrix} A_\theta & X & R \end{pmatrix}; \qquad \bar{\boldsymbol{\alpha}}^r = \begin{pmatrix} \alpha_\theta^r \\ \beta^r \\ \gamma^r \end{pmatrix} \\ \mathbf{M}_\theta &= \begin{pmatrix} M_\theta & 0 & 0 \\ 0 & \eta M_X & 0 \\ 0 & 0 & M_R \end{pmatrix}; \end{aligned} \tag{25}$$

Finally, as previously, two operators are introduced: T_θ is the discrete trace operator on $\partial\omega_\theta$ and C_θ is such that $C_\theta \bar{\boldsymbol{\alpha}}^r \leqslant 0$ ensures that $[\![\underline{u}_r]\!] \geqslant 0$ on any point of Σ, which is the non-interpenetration condition between the faces of the crack. Our final minimization problem can be written as:

$$\begin{aligned} \min_{\theta,(T_\theta\bar{\boldsymbol{\alpha}}^r=0, C_\theta\bar{\boldsymbol{\alpha}}^r\leqslant 0)_{r=1\dots r_{\max}}} & \frac{1}{2}\sum_{r=1}^{r_{\max}} \left(\bar{\boldsymbol{\alpha}}^{rT}\left(\mathbf{A}_\theta^T\mathbf{A}_\theta + \mu\mathbf{M}_\theta^T\mathbf{M}_\theta\right)\bar{\boldsymbol{\alpha}}^r\right. \\ & \left. - \bar{\boldsymbol{\alpha}}^{rT}\mathbf{A}_\theta^T b^r\right) \end{aligned} \tag{26}$$

Remark 6 *As it is used here, the Reciprocity Gap method reconstructs a field (the displacement gap) which is an indicator of the presence of a crack. From this point of view, it is close to the topological gradient method [2] and the linear sampling method [15]. The first method uses the topological gradient as such indicator, and the second is a method in inverse scattering theory based on solving a linear integral equation that*

uses the equation's solution as an indicator function for the the support of the scattering object.

5.2 Technical choices

Note that all remarks given in Section 4.2 are also relevant for this approach, but other topics need to be considered.

- The regularization parameter η was introduced for physical homogeneity reasons. In practice it can be fixed such that $(\|M_\theta\|_F^2 + \|M_R\|_F^2) \simeq \eta \|M_X\|_F^2$.
- The same balancing should be carried on for the matrices Φ_θ, R and X. X is replaced by λX such that $(\|\Phi_\theta\|_F^2 + \|R\|_F^2) \simeq \lambda \|X\|_F^2$ (and as a post process operation, β^r is multiplied by λ).
- As previously, the surface ω_θ is meshed, and finite element shape functions are used for $(\phi_{\theta,j})$. Regarding the boundary quantities, the parts bearing unknowns are also meshed. The force $\underline{\widetilde{f}}_r$ is approximated by piecewise constant functions, whereas the displacement $\underline{\widetilde{u}}_r$ is approximated by continuous piecewise linear functions.
- Provided the regularization parameter is well-chosen, the result on the crack's plane ω_θ is mesh-independent, which means that the shape of the solution does not depend on the mesh size, and only the resolution is impacted. On the contrary, it has been observed that a too coarse mesh of $\partial\Omega$ can lead to instabilities in the identification of the displacement jump on ω_θ. This is probably due to the fact that if not enough degrees of freedom were available on $\partial\Omega$ to describe properly the boundary fields, the algorithm would artificially reduce the residual by proposing an irrelevant displacement jump field on ω_θ. For that reason, it is recommended to use a coarser mesh on ω_θ than on $\partial\Omega$. Let us emphasize the fact that, in the part dedicated to the numerical results, this mesh is finer than necessary in order to make the result more readable.
- As said earlier, part of the problem does not vary with the position of the plane, which can be exploited to reduce the computational cost. Let us study the matrix of the system:

$$\mathbf{D} = \mathbf{A}_\theta^T \mathbf{A}_\theta + \mu \mathbf{M}_\theta^T \mathbf{M}_\theta = \left(\begin{array}{c:cc} A_\theta^T A_\theta + \mu M_\theta & A_\theta^T X & A_\theta^T R \\ \hdashline & X^T X + \mu\eta M_X^T M_X & X^T R \\ \text{sym} & & R^T R + \mu M_R^T M_R \end{array}\right) \tag{27}$$

Let us note with subscript θ the first block (which depends on the crack plane), and with subscript b the second block which is invariant (b stands for boundary). For each configuration θ, the system to be solved takes the form:

$$\begin{pmatrix} D_{\theta\theta} & D_{\theta b} \\ D_{b\theta} & D_{bb} \end{pmatrix} \begin{pmatrix} x_\theta \\ x_b \end{pmatrix} = \begin{pmatrix} y_\theta \\ y_b \end{pmatrix} \tag{28}$$

which we organize the following way:

$$\begin{aligned} \left(D_{\theta\theta} - D_{\theta b} D_{bb}^{-1} D_{b\theta}\right) x_\theta &= y_\theta - D_{\theta b} D_{bb}^{-1} y_b \\ x_b &= D_{bb}^{-1}(y_b - D_{b\theta} x_\theta) \end{aligned} \tag{29}$$

The assembly and factorization of D_{bb} is done once for all. What remains to be computed at each iteration is the Schur complement (first line of (29)) which is of small dimension.

Moreover, using the Uzawa algorithm to take care of the non-penetration constraint is particularly efficient on the condensed system: x_b needs not be updated every time, and the smallest eigenvalue of the condensed system (which drives the convergence) is greater than the one of the original system.

5.3 Numerical study

As for the previous numerical experiment, the measurements were interpolated on a coarser mesh before being used.

On this example, the stagnation of the cost-function Φ happens after 6 iterations. Figure 16 shows the identified crack's line. As for the PG0-RG method, this line is very close to the reference line of the crack. Table 2 shows the error on identified displacement jump and Neumann reaction on the top boundary. Given those results, it was chosen to display graphically only the identification resulting from load cases 1 and 4 (see Figure 18b). The quality of the reconstruction appears to be comparable to that of the PG0-RG method. The load-case 2, that is nearly parallel to the crack's line, induces a displacement jump of very small magnitude that is not identifiable by this method.

Furthermore, it is possible to identify the reaction force on the boundary with missing Neumann data, as displayed on Figure 18a. On this reaction force, the result is less accurate than the result obtained via the resolution of a Cauchy problem (see Figure 6). This is due to the fact that the regularization coefficient has been determined by plotting a L-curve considering only the norm of the displacement jump on the crack line, and not this reaction force.

5.4 Conclusion on the gPG-RG method

This method identifies simultaneously the crack and the missing boundary conditions. It has the advantage to rely on very few assumptions. Regularization seems to perform quite well, leading to good quality results.

The method requires to do many partial assemblies of surface quantities and inversions of small but dense matrices. In simple geometry cases, the solution of the inverse problem via the reciprocity gap method can even be faster than the forward cracked problem. On the other hand, cases can be found, with complex boundaries and many missing data, where the method is numerically very expensive.

6 Numerical investigation of the gPG-RG method

In this part, the gPG-RG method presented in Section 5 is assessed on various test-cases based on the same geometry as previously. The first parameter that can vary is the number of sensors on the boundary of the studied domain. As a matter of fact, it is expected that the fewer sensors are present, the less precise the identification will be. Then, the stability of the method with respect to an additive Gaussian noise on the Dirichlet data is investigated.

Load case	1	2	3	4
Relative error on the extra BC identification	0.097940	0.48754	0.21947	0.14691
Relative error on the displacement jump identification	0.22109	2.5757	0.97297	0.37512

Table 2: Errors of the identification procedure – gPG-RG method (Section 5)

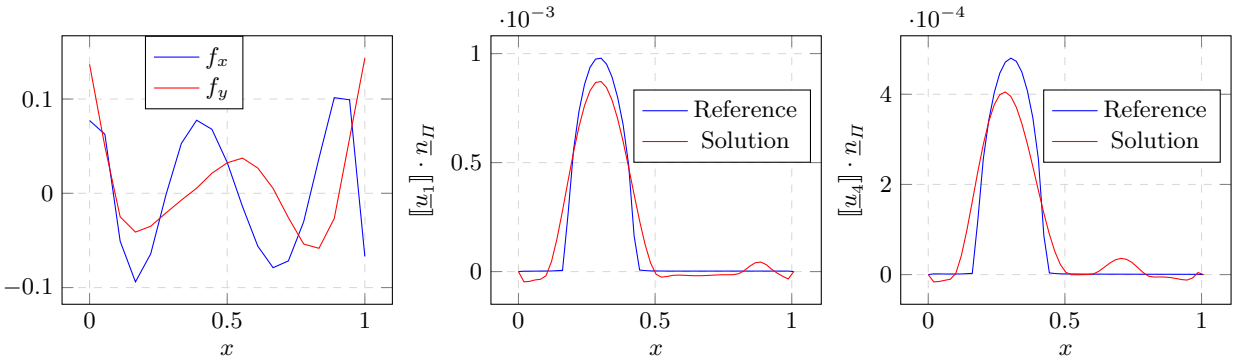

(a) Pointwise relative error on the identified reaction force

(b) Identification of the normal displacement jump

Fig. 18: Identification of the reaction force and the normal displacement jump – gPG-RG method (Section 5)

Unknown Dirichlet	Unknown Neumann	Noise level	Error $r=1$	Error $r=2$	Error $r=3$	Error $r=4$
-	Top	0	0.22109	2.5757	0.97297	0.37512
-	Bottom and Top	0	0.85649	1.7539	2.2508	0.58149
-	Right and Top	0	0.56698	9.8960	1.8935	1.2769
Top	Top	0	0.27089	0.39863	0.45479	0.30697
Pointwise	Top	0	0.61730	0.81833	0.60565	0.72947
Top	Top	1 %	0.51328	0.75323	0.58504	0.37015
Top	Top	5 %	0.77818	2.3261	1.0576	2.2263

Table 3: Summary of the errors on the displacement jump identification (section 6)

6.1 Effect of the number of sensors

In this part, the impact of the number of measure points is studied.

In the first experiment, Neumann data are missing on both top and bottom boundaries. It can be remarked from the analysis of Figure 19 that the orientation of the crack is not recovered accurately in this case. However, it is noticeable, that the displacement jump, that gives the position of the crack in its line, is quite well reconstructed (at least for the load-

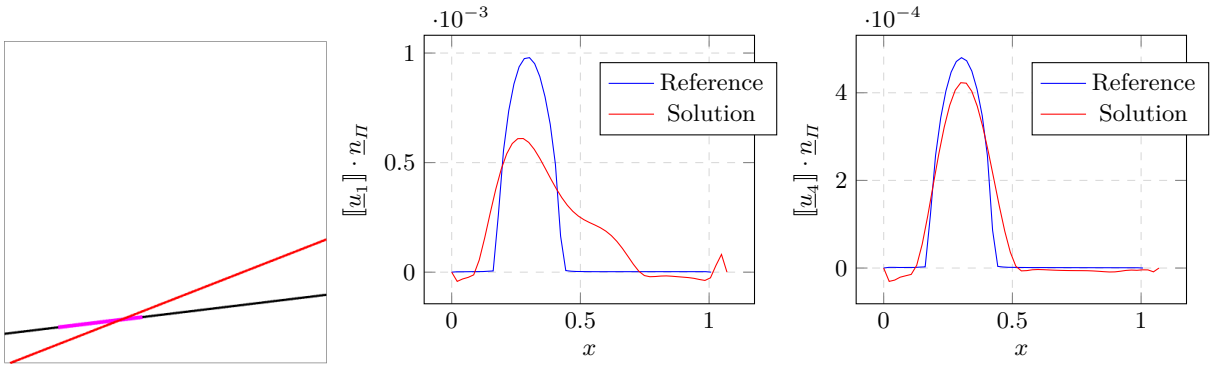

Fig. 19: Identification of the crack's line and the normal displacement jump in the case of top and bottom Boundaries missing Neumann data (using loads $r = 1$ and $r = 4$).

cases with the greatest jump amplitude). The relative bad quality of those results is probably due to the fact that the crack is in fact close to one of the boundaries where no Neumann data is available. That is why another setting is tried, on which the two boundaries where Neumann data is missing are the right and top ones, that are far from the real position of the crack.

On Figure 20, we can see that the line of the crack is better reconstructed, and Figure 20 presents acceptable reconstructions for the load-cases 1 and 4, that lead to the greatest amplitudes of the gap.

In the third experiment, both Dirichlet and Neumann data are missing on top boundary. This case is such that $\Gamma_n \cup \Gamma_d \neq \partial\Omega$. On Figure 21, it is noticeable that the identification of the line is very good. We see that the quality of the identification of the displacement jump is comparable with the quality obtained on Figure 18b. This good result can be explained again by the position of the crack, that is far away from the boundary with missing data.

Finally, in the last test-case, all the Neumann data is available (except on the top boundary) and only pointwise Dirichlet conditions are known. It has been chosen to use one measure point per corner and 4 extra points regularly distributed on each segment, while the mesh used for the computation of the reciprocity gap has 146 nodes on the boundary.

From the analysis of Figure 22, it can be said that the orientation of the crack is rather badly identified. However, as the identified line intersects the reference line quite close to the real position of the crack, the position of the crack itself is roughly correct. What is more, the reconstructed displacement jump is much smoother than the reference jump (while the value of the regularization parameter is the same as for the previous computations). This can be explained by the fact that as there are less known data, the impact of the regularization term is increased. This last numerical experiment shows that while the proposed method is theoretically able to deal with pointwise Dirichlet data, it is not very efficient in practice.

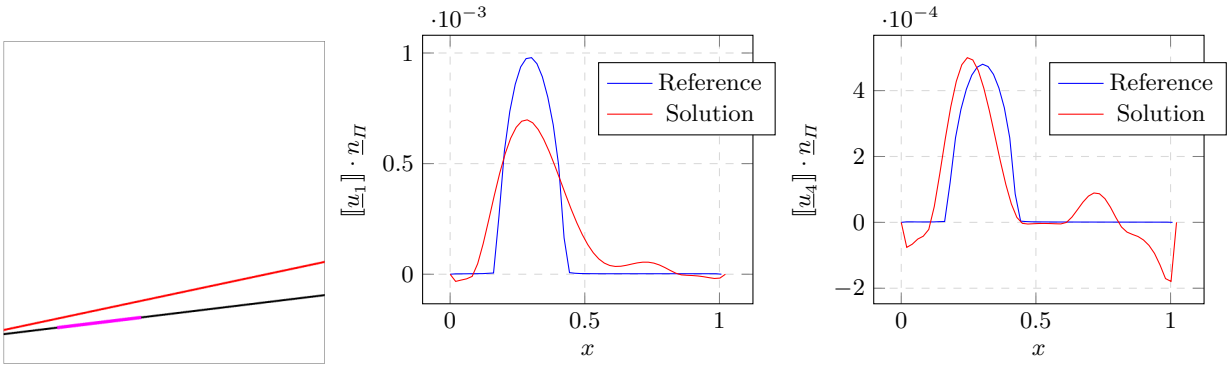

Fig. 20: Identification of the crack's line and the normal displacement jump in the case of right and top Boundaries missing Neumann data (using loads $r = 1$ and $r = 4$).

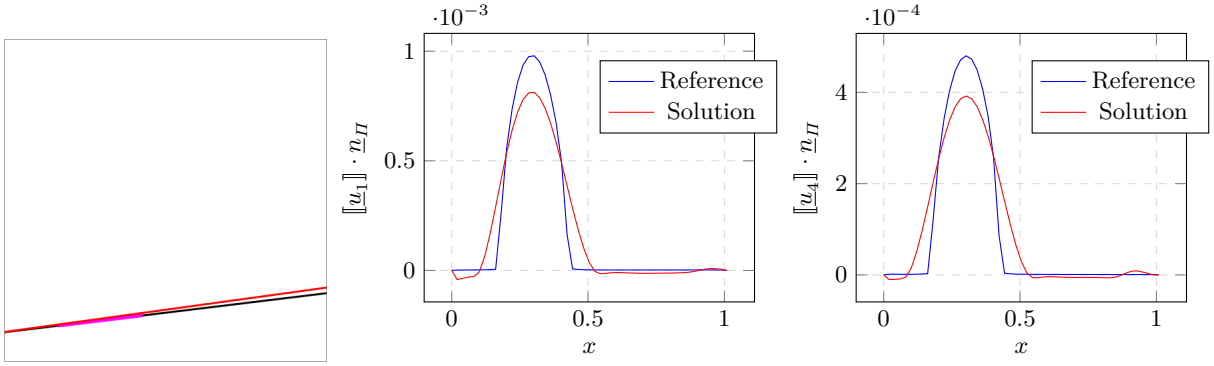

Fig. 21: Identification of the crack's line and the normal displacement jump in the case with no data on top Boundary

6.2 Impact of the noise level

In this part, Dirichlet and Neumann data are missing on the top boundary. In the first case, the noise level is 1 % on the Dirichlet data. The Tikhonov regularization parameter was consequently increased for this test-case. The analysis of Figure 23 shows that the identification of the line of the crack is perturbed by the noise. We can observe that the reconstruction of the displacement jump is smoothed by the increase of the regularization parameter, but its localization is still rather well identified.

Another numerical experiment is carried out with a higher noise level (5 %). As previously, the Tikhonov parameter was again increased. As expected, the quality of the reconstructed crack's line, presented on Figure 24 decreases. However, the identified gaps still give a rough idea of the real localization of the crack.

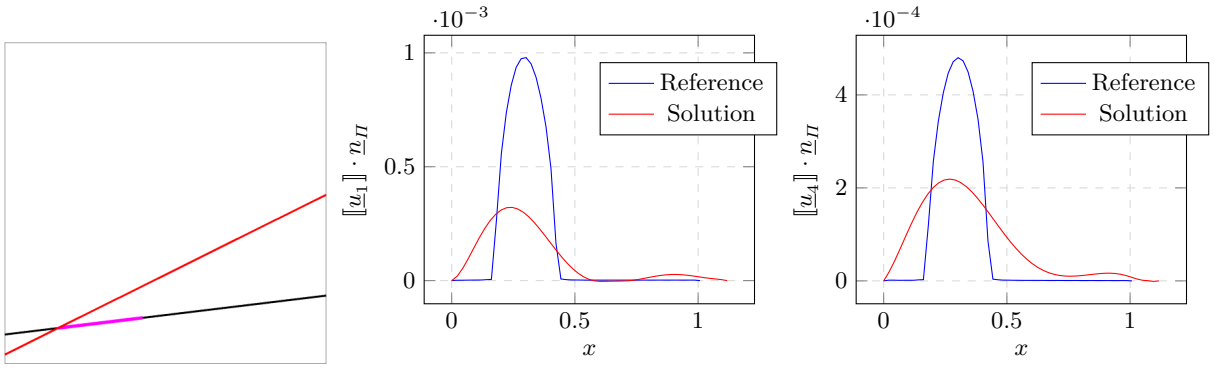

Fig. 22: Identification of the crack's line and the normal displacement jump in the case with Neumann missing data on top boundary and only pointwise Dirichlet data

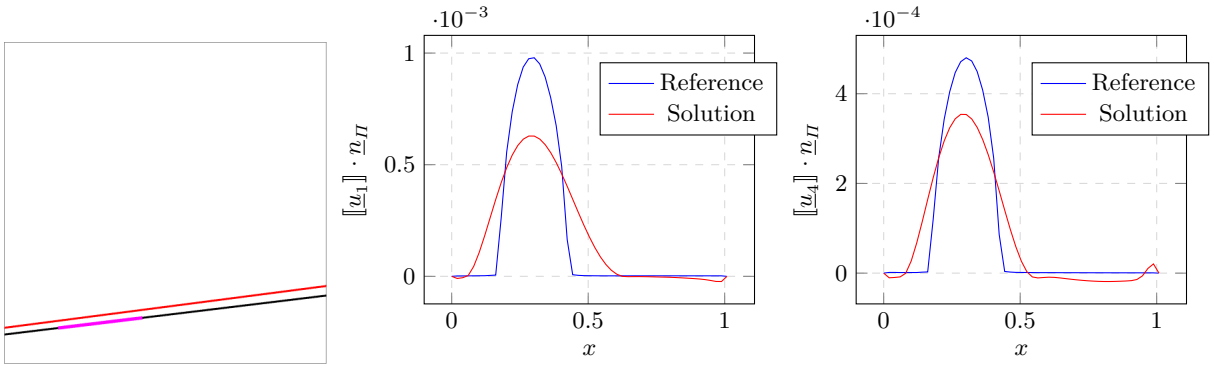

Fig. 23: Identification of the crack's line and the normal displacement jump with 1 % gaussian noise on the Dirichlet data

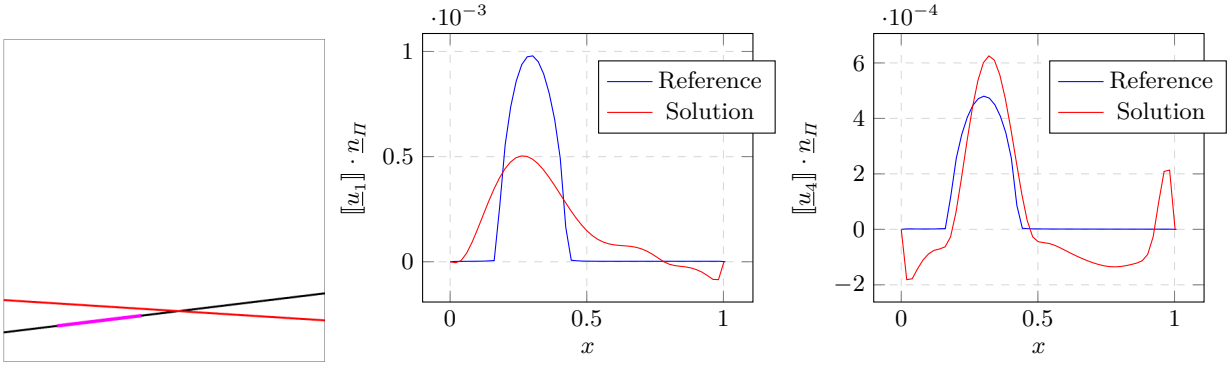

Fig. 24: Identification of the crack's line and the normal displacement jump with 5 % gaussian noise on the Dirichlet data

7 Numerical experiment on a 3D case

In this part, we show the behavior of the simultaneous identification algorithm on a more demanding 3D case with a crack that is distant from any boundary.

We consider the unit cube, with an internal elliptic crack. The cube is submitted to a zero Dirichlet boundary condition on its top face, and is submitted sequentially to 13 different traction loads, that are the 3D analogs to the load-cases presented on Figure 3. The 13 forward problems that result from those loads are solved and the full solutions are stored. As previously, the data is redundant on all the boundary of the domain, except on the top boundary where Neumann data is not available. Again, the boundary mesh used for the computation of the integrals (inverse problem) is not coincident with the boundary of the mesh used for the simulation of the experiments (forward problem), and interpolation is performed to transfer the simulated measurements from the second to the first one. Moreover, 1 % extra synthetic Gaussian noise was added.

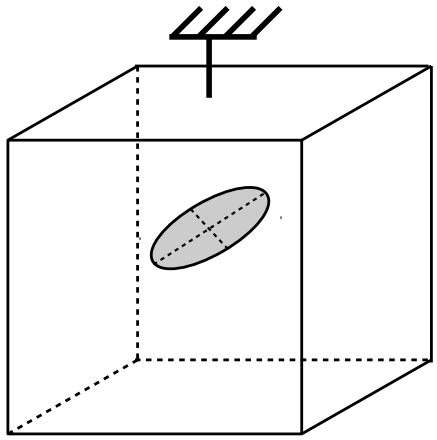

Fig. 25: Setting of the domain with the Dirichlet boundary conditions and the elliptic crack for the direct problem

1323 test functions are used (polynoms of $\mathcal{V}$ of degree at most 20). There are 9948 degrees of freedom for the reaction force on the boundary $\Gamma_{\overline{n}}$, and about 2000 degrees of freedom for the displacement gap on ω (this number changes at every iteration as the surface moves). The total duration of the computation is 2428 seconds: 699 for the computation of the right and left hand sides, 143 for the assembly and factor-

ization of D_{bb} (see (29)), and 176 seconds are required per Newton iteration.

The computation has been carried out on a computer with 8 CPU @ 1.60GHz, and about 10Go of RAM has been used.

For information, the direct problem was solved using a mesh with 88016 nodes (and thus 264048 degrees of freedom), and the resolution of the 13 contact problems by multiple right-hand side required about 30 minutes with our implementation.

The regularization parameter is determined manually by testing different values and keeping the lowest value before strong oscillations appear. The resulting value is 100.

The residual stagnates after 9 iterations, and at this point, the identified plane, on Figure 26, is quite close to the reference plane, and the displacement jump identified on this plane, presented on the same figure for one of the 13 load cases, is comparable to the reference: the identified crack is slightly deformed, but its position and size are quite accurate, as well as the value of the maximum of the gap.

It can be proposed to apply a threshold to the identified normal gap (chosen to 20% of the maximal value in our example) in order to reconstruct the crack itself. The outcome of this process is displayed on Figure 28.

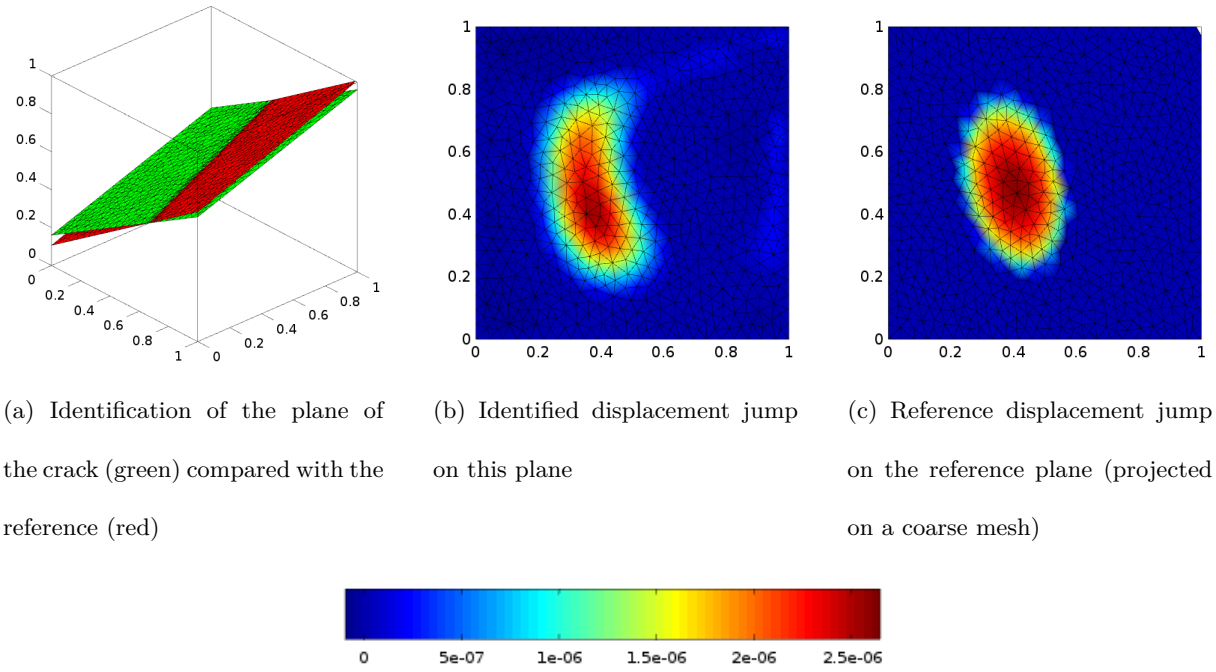

(a) Identification of the plane of the crack (green) compared with the reference (red)

(b) Identified displacement jump on this plane

(c) Reference displacement jump on the reference plane (projected on a coarse mesh)

Fig. 26: Identification of the crack with 1 % added Gaussian noise

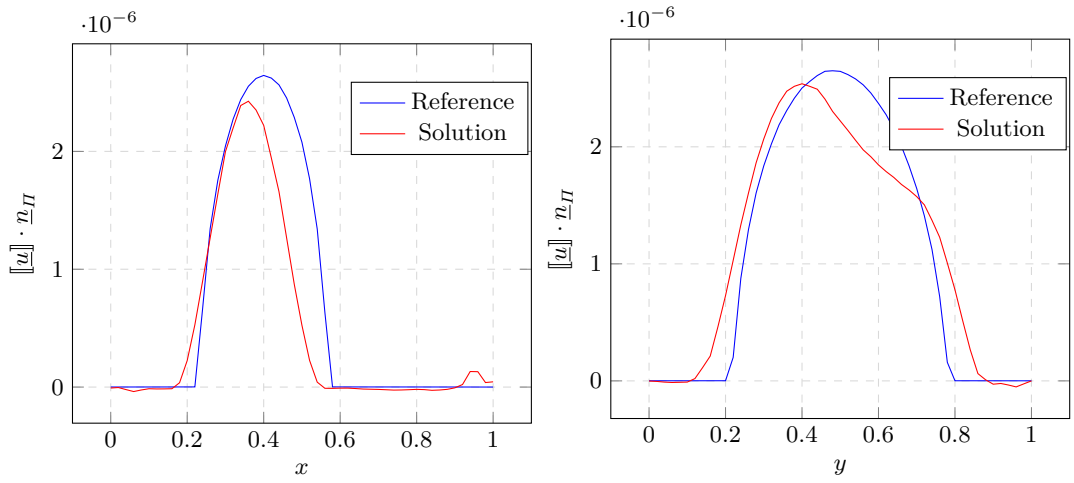

Fig. 27: Normal displacement jump plotted on the line $y = .5$ (left) and $x = .4$ (right)

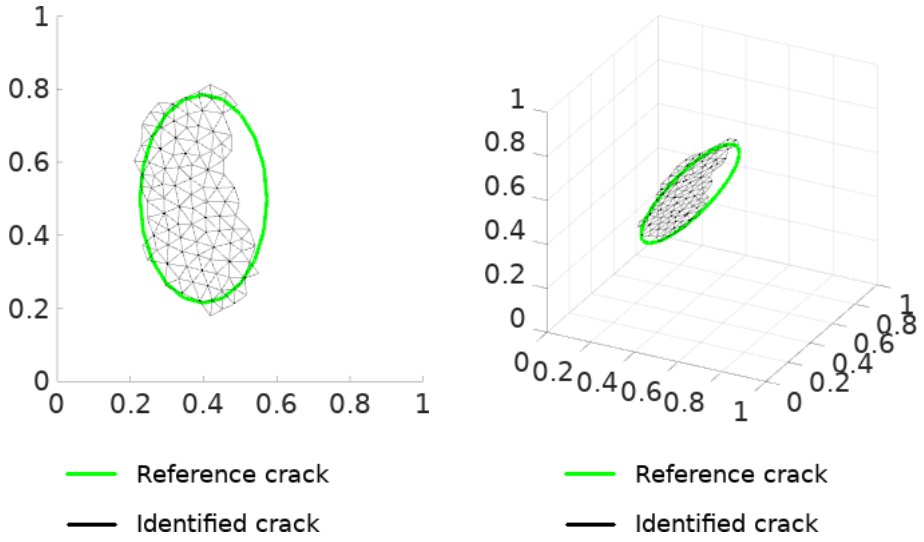

Fig. 28: Identification of the shape of the crack by thresholding

Conclusion and perspectives

In this paper, three methods have been proposed and tested to overcome the classical limitation of the reciprocity gap method which needs redundant Dirichlet and Neumann data on the entire boundary. The first method, referred as C-RG, consists in preprocessing the data by solving a Cauchy problem; it turned out to be applicable only in adapted cases (see for example [4]). The second method, referred as PG0-RG, which consists in adapting the test-functions is only suited for simple shapes of the boundary, but in those cases, it is potentially very efficient in terms of CPU and accuracy. The last method, referred as gPG-RG, is more general and can be applied in cases where the shape of the boundary with missing data is arbitrarily complex.

This gPG-RG method was then illustrated and numerically tested using data of various quantity and quality, and on a 3D plane crack identification testcase.

Finally, the proposed methods introduce a set of variable parameters, like the number of Uzawa iterations, the maximum order of the polynomial test functions and the regularization coefficients. Defining tuning strategies is the main perspective of this work.

A Brief study of the Petrov-Galerkin formulation

This appendix aims at providing some theoretical ground to the formulation used in Sections 4 and 5. For simplicity reasons, we focus on the case of identifying a crack with fully known boundary conditions. The extra terms needed for more general cases do not change the main properties of the system.

We recall that the system to be solved takes the form (for simplicity reason, we drop the subscript r,

and the bracket notations for the displacement jump):

$$\begin{gathered}\text{Find } \underline{u} \in H_{00}^{1/2}(\omega), \text{ such that } \forall \underline{v} \in \mathcal{V}, \\ \langle \underline{\underline{\sigma}}(\underline{v}) \cdot \underline{n}, \underline{u} \rangle_{H^{1/2}(\omega)} = \int_{\partial\Omega} \widehat{\underline{f}} \cdot \underline{v} - \widehat{\underline{u}} \cdot \underline{\underline{\sigma}}(\underline{v}) \cdot \underline{n} \, dS\end{gathered} \tag{30}$$

with

$$\mathcal{V} = \left\{ \underline{v} \in H^1(\Omega), \underline{\underline{\sigma}}(\underline{v}) \in H_{div}(\Omega), \mathrm{div}(\underline{\underline{\sigma}}(\underline{v})) = 0 \right\} \tag{31}$$

In the formulation, we make use of the duality bracket in the Hilbert space $H_{00}^{1/2}$. $\mathcal{V}$ is a closed subspace of $H^1(\Omega)$, it inherits its Hilbert space structure. Fields in $\mathcal{V}$ have enough regularity for the trace and normal flux to be well-defined and continuous on the boundary and on ω, so that all operations are well posed and the (bi)linear forms are continuous. In practice, we use polynomial approximation in $\mathcal{V}$ and Lagrange finite element in $H_{00}^{1/2}$, granting sufficient regularity to replace the duality bracket by a classical integral on ω.

Formulation (30) makes use of different search ($H_{00}^{1/2}$) and test ($\mathcal{V}$) spaces, which is the playground of the Banach-Necas-Babŭska theorem [17], also known as inf-sup theorem.

One first precaution must be taken. For a given plane surface ω, we can define $\mathcal{V}_\omega$, the space of the $\underline{v}$ such that $\underline{\underline{\sigma}}(\underline{v}) \cdot \underline{n}|_\omega = 0$. Let us define $\underline{v} \in \mathcal{V}_\omega^\perp$, the subspace of $\mathcal{V}$ that is orthogonal to $\mathcal{V}_\omega$. $\mathcal{V}_\omega$ is a closed space, which means in particular that it is not dense in $\mathcal{V}$, and ensures that $\underline{v} \in \mathcal{V}_\omega^\perp$ is not empty. In order to avoid inconsistency, the formulation must be studied with $\underline{v} \in \mathcal{V}_\omega^\perp$.

For the formulation to be stable, the following quantity should be bounded from below by a positive number:

$$\inf_{\underline{u} \in H_{00}^{1/2}(\omega)} \sup_{\underline{v} \in \mathcal{V}_\omega^\perp} \frac{\langle \underline{\underline{\sigma}}(\underline{v}) \cdot \underline{n}, \underline{u} \rangle}{\|\underline{u}\|_{H^{1/2}(\omega)} \|\underline{v}\|_{\mathcal{V}}} \tag{32}$$

Unfortunately, this is not possible. Indeed, we have the following property:

$$\inf_{\underline{u} \in H_{00}^{1/2}(\omega)} \sup_{\underline{\tau} \in H^{-1/2}(\omega)} \frac{\langle \underline{\tau}, \underline{u} \rangle}{\|\underline{u}\|_{H^{1/2}(\omega)} \|\underline{\tau}\|_{H^{-1/2}(\omega)}} = 1 \tag{33}$$

and more precisely, for a given $\underline{u} \in H_{00}^{1/2}$, the $\underline{\tau}$ which realizes the upper bound is the image of $\underline{u}$ by Riesz' isomorphism which we note $\underline{\tau}_{\underline{u}}$. The problem is then to find $\underline{v} \in \mathcal{V}$ such that $\underline{\underline{\sigma}}(\underline{v}) \cdot \underline{n} = \underline{\tau}_{\underline{u}}$; this is the subject of Proposition 2. Unfortunately, its proof appeals to a Cauchy problem, which is unstable. Thus we can not control $\|\underline{v}\|_{\mathcal{V}}$ from above with $\|\underline{\tau}_{\underline{u}}\|_{H^{-1/2}} = \|\underline{u}\|_{H_{00}^{1/2}}$.

In the end, the lack of stability is caused by fields $\underline{u} \in H_{00}^{1/2}(\omega)$ aligned with high energy test fields $\underline{v} \in \mathcal{V}_\omega^\perp$. This justifies the use of gradient-based regularization.

Proposition 2 *Let ω be a surface that cuts the domain Ω. For any $\underline{\tau} \in H^{-1/2}(\omega)$, there exists $\underline{v} \in \mathcal{V}_\omega^\perp$ such that $\underline{\underline{\sigma}}(\underline{v}) \cdot \underline{n}_\Pi = \underline{\tau}$ on ω.*

Proof The surface ω splits Ω into two open sets, denoted by Ω_1 and Ω_2. For any $\underline{u}_1 \in H^{1/2}(\partial\Omega_1)$, one can solve a direct problem on Ω_1 in order to build $\underline{v}_1 \in H^1(\Omega_1)$ such that the equilibrium s verified and $\underline{\underline{\sigma}}(\underline{v}_1) \cdot \underline{n}_\Pi = \underline{\tau}$ on ω.

$\underline{v}_1$ and $\underline{\tau}$ are compatible data for a Cauchy problem set on Ω_2, and it is possible to build the field $\underline{v}_2 \in$

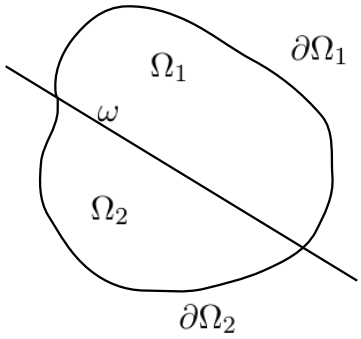

Fig. 29: Splitting of the domain

$H^1(\Omega_2)$ such that the equilibrium is also verified and $\underline{\underline{\sigma}}(\underline{v}_2) \cdot \underline{n}_{\Pi} = \underline{\tau}$ on ω.

The traces on ω of the fields $\underline{v}_1$ and $\underline{v}_2$ are the same, and consequently, the field $\underline{v}$, that is equal to $\underline{v}_1$ on Ω_1 and $\underline{v}_2$ on Ω_2, and that is extended by continuity on ω, is in $\mathcal{V}_{\omega}^{\perp}$ and is such that $\underline{\underline{\sigma}}(\underline{v}) \cdot \underline{n}_{\Pi} = \underline{\tau}$ on ω.

References

1. G. Alessandrini, L. Rondi, E. Rosset, and S. Vessella. The stability for the cauchy problem for elliptic equations. *Inverse problems*, 25(12):123004, 2009.
2. S. Amstutz, I. Horchani, and M. Masmoudi. Crack detection by the topological gradient method. *Control and Cybernetics*, 34(1):81–101, 2005.
3. S. Andrieux. The reciprocity likelihood maximization: a variational approach of the reciprocity gap method. *Journal of mechanics of materials and structures*, 10(3):219–237, 2015.
4. S. Andrieux and T. Baranger. Emerging crack front identification from tangential surface displacements. *Comptes Rendus Mécanique*, 340(8):565–574, 2012.
5. S. Andrieux, T. Baranger, and A. Ben Abda. Solving Cauchy problems by minimizing an energy-like functional. *Inverse problems*, 22(1):115, 2006.
6. S. Andrieux and A. Ben Abda. The reciprocity gap: a general concept for flaws identification problems. *Mechanics research communications*, 20(5):415–420, 1993.
7. S. Andrieux, A. Ben Abda, and H. D. Bui. Reciprocity principle and crack identification. *Inverse problems*, 15(1):59, 1999.
8. S. Andrieux, A. Ben Abda, and M. Jaoua. On the inverse emergent plane crack problem. *Mathematical Methods in the Applied Sciences*, 21(10):895–906, 1998.
9. S. Avril, M. Bonnet, A.-S. Bretelle, M. Grediac, F. Hild, P. Ienny, F. Latourte, D. Lemosse, S. Pagano, E. Pagnacco, et al. Overview of identification methods of mechanical parameters based on full-field measurements. *Experimental Mechanics*, 48(4):381, 2008.
10. A. Ben Abda, H. B. Ameur, and M. Jaoua. Identification of 2D cracks by elastic boundary measurements. *Inverse Problems*, 15(1):67, 1999.
11. A. Ben Abda, F. Delbary, and H. Haddar. On the use of the reciprocity-gap functional in inverse scattering from planar cracks. *Mathematical Models and Methods in Applied Sciences*, 15(10):1553–1574, 2005.
12. A. Ben Abda, M. Kallel, J. Leblond, and J.-P. Marmorat. Line segment crack recovery from incomplete boundary data. *Inverse Problems*, 18(4):1057, 2002.
13. F. Ben Belgacem. Why is the Cauchy problem severely ill-posed? *Inverse Problems*, 23(2):823–836, 2007.
14. F. Ben Belgacem and H. El Fekih. On Cauchy's problem: I. A variational Steklov–Poincaré theory. *Inverse Problems*, 21(6):1915, 2005.

15. F. Cakoni and D. Colton. The linear sampling method for cracks. *Inverse problems*, 19(2):279, 2003.

16. A. Cimetiere, F. Delvare, M. Jaoua, and F. Pons. Solution of the Cauchy problem using iterated Tikhonov regularization. *Inverse Problems*, 17(3):553–570, 2001.

17. A. Ern and J.-L. Guermond. *Theory and practice of finite elements*, volume 159. Springer Science & Business Media, 2013.

18. R. Ferrier, M. L. Kadri, and P. Gosselet. The Steklov-Poincaré technique for data completion: Preconditioning and filtering. *International Journal for Numerical Methods in Engineering*, 116(4):270–286, 2018.

19. R. Ferrier, M. L. Kadri, and P. Gosselet. Planar crack identification in 3D linear elasticity by the Reciprocity Gap method. *Computer Methods in Applied Mechanics and Engineering*, 355:193–215, 2019.

20. C. Geuzaine and J.-F. Remacle. Gmsh: A 3-D finite element mesh generator with built-in pre-and post-processing facilities. *International journal for numerical methods in engineering*, 79(11):1309–1331, 2009.

21. M. L. Kadri, J. Ben Abdallah, and T. Baranger. Identification of internal cracks in a three-dimensional solid body via Steklov–Poincaré approaches. *Comptes Rendus Mécanique*, 339(10):674–681, 2011.

22. V. A. Kozlov and V. G. Maz'ya. Iterative procedures for solving ill-posed boundary value problems that preserve the differential equations. *Algebra i Analiz*, 1(5):144–170, 1989.

23. D. P. O'Leary. The block conjugate gradient algorithm and related methods. *Linear algebra and its applications*, 29:293–322, 1980.

24. F. Santosa and M. Vogelius. A computational algorithm to determine cracks from electrostatic boundary measurements. *International journal of engineering science*, 29(8):917–937, 1991.

25. E. Shifrin and P. Shushpannikov. Identification of small well-separated defects in an isotropic elastic body using boundary measurements. *International Journal of Solids and Structures*, 50(22):3707–3716, 2013.

26. E. I. Shifrin and A. V. Kaptsov. Identification of multiple cracks in 2D elasticity by means of the reciprocity principle and cluster analysis. *Inverse Problems*, 34(1):015009, 2017.

27. P. Steinhorst and B. Kaltenbacher. Application of the reciprocity principle for the determination of planar cracks in piezoelectric material. In *Advanced Finite Element Methods and Applications*, pages 325–353. Springer, 2013.